Simulation of soil-to-tool interaction using Discrete Element Method (DEM) and Multibody Dynamics (MBD) coupling

by

Sadaf Ghorbani

A thesis submitted to the graduate faculty

in partial fulfillment of the requirements for the degree of

MASTER OF SCIENCE

Major: Agricultural and Biosystems Engineering

Program of Study Committee:
Mehari Z. Tekeste, Major Professor
Stuart Birrell
Brian Steward
Adam Thoms

Iowa State University

Ames, Iowa

2019

DEDICATION

To

my husband, Mohammad,

who supported and encouraged me in every step of the way through completion of this work

TABLE OF CONTENTS

ACKNOWLEDGMENTS

I would like to first and foremost thank my major professor, Dr. Mehari Tekeste whose continuous support and guidance made the completion of my research possible. I am genuinely grateful for his extensive knowledge, incredible patience and endless encouragement through my time in graduate school. I also wish to thank my thesis committee members, Dr. Stuart Birrell, Dr. Brian Steward and Dr. Adam Thoms for their helpful advice and recommendations through my research. I also want to express my gratitude to Catherine Horak at Siemens for providing training and continuous support in using their software package. I would also like to thank my fellow graduate students for their feedback and cooperation. I wish to especially thank Dylan Childs for dedicating his time and efforts to assist me with completing the physical experiments.

ABSTRACT

Multi-physics simulation of soil-to-tool interaction using a coupled Discrete Element Method (DEM) and Multibody dynamics (MBD) techniques can support the design of off-road equipment. Quantitative prediction of the soil reaction forces on the equipment is essential to provide a reliable simulation-based design. DEM is a computational method for simulating the dynamic behavior of granular materials. In the coupling interface, DEM gives a high fidelity prediction of the forces for soil-to-soil and soil-to-tool interaction, which can be used in the MBD simulation workflow. Two laboratory tests were used to capture the bulk material behavior: the angle of repose test for calibration of coefficients of static friction and rolling friction, and the cone penetrometer test to calibrate the soil shear modulus and normal and shear stiffnesses (related to the Hertz-Mindlin with bonding contact model). A simple pendulum test was developed to validate the DEM soil model in a soil-to-tool interaction application. The test was conducted in a soil bin filled loosely with loam soil at soil moisture content of 10% and initial soil bulk density of $1330 \, \text{kg/m}^3$. A cutting plate connected to the pendulum cut the soil at two levels of cutting depths (25 mm and 50 mm). The same application was simulated using the DEM simulation and DEM-MBD co-simulation. The horizontal and vertical soil cutting forces were compared between simulations and test. The magnitude of the maximum horizontal cutting forces for the experiment, DEM simulation, and DEM-MBD co-simulation were 73 N, 365 N, and 187 N, respectively for the 25 mm cutting depth and 108 N, 766 N, and 278 N, respectively for the 50 mm cutting depth. The DEM-MBD coupling improved the force prediction both for 25 mm and 50 mm cutting depths. It also closely predicted the trend in the increase in horizontal forces by cutting depth. The maximum horizontal soil cutting forces from experiment and DEM-MBD co-simulation increase by 48% and 49% by increasing the depth, respectively.

CHAPTER 1. INTRODUCTION

The worlds population was reported as 7.6 billion in 2017 and is predicted to grow to 9.8 billion by 2050 (UN, 2017). To ensure the continuous food supply for the growing population, an efficient and productive agricultural system is required. Tillage has been used for thousands of years to increase food production by mechanically manipulating the soil to prepare it for seedling establishment and root growth. Tillage is one of the most expensive and power consuming part of the agricultural field operation, requiring 180 to 320 kW power per hectare, which is equal to 50 to 80 kg of fuel per hectare tilled (Vilde, 2003). Thus, the tillage equipment should be the most efficient, and provide the desirable soil quality for plant growth with the minimum amount of power and fuel consumption. Simulation-based design offers the opportunity to accelerate the design and performance evaluation of the tillage equipment.

To provide a reliable simulation-based design for tillage tools, it is crucial to quantify the soil dynamic responses under loading from the tillage tools. Measurement of soil flow and soil reaction forces should be considered when selecting or designing a tillage tool due to their effects on power and fuel consumption (Godwin, 2007). It is often expensive and time consuming to create multiple physical prototypes and perform field tests in order to measure the soil reaction forces and the soil tilth quality. Leveraging empirical, analytical, or numerical methods that model the soil-to-tool interactions and integrating the methods into engineering design workflow has shown to be a preferable approach.

Many empirical formulas have been developed (Larson et al., 1968; Luth and Wismer, 1971; Wismer and Luth, 1972) to predict soil reaction force. The drawback of these formulas is that they are limited to a specific tool geometry and the experimental soil conditions. Passive earth pressure-based analytical methods have also been utilized to predict the soil reaction forces (Hettiaratchi et al., 1966; McKyes and Ali, 1977). Those analytical methods are relatively accurate to predict

the soil reaction forces; however, they are limited to quasi-static simple tool motion and assume the soil as a continuum medium. In fact, soil is a granular material, and by assuming it as a continuum body, these methods were not able to predict the soil deformation and soil flow under typical tillage loading conditions.

Numerical methods and the virtual experiments are more accurate and efficient ways to use in soil-to-tool interaction modeling. Finite Element Method (FEM) is a numerical method which has been used in soil-to-tool modeling, and successfully modelled relatively small volumetric strain in soil-to-tool interaction problems. However, in tillage applications, agricultural soils deform in larger volumetric strain. Therefore, numerical techniques that predict various soil deformation phases such as elasto-plastic compression, shearing and discretized soil particles flow are more suitable for simulating realistic soil-to-tool interaction. Discrete Element Method (DEM) is a robust numerical method which simulates the dynamic behavior of discontinuing granular material. This method, which was introduced by Cundall and Strack (1979) has become a useful computational technique in process manufacturing, mining, construction and agricultural industries. The discreteness of the DEM method makes it suitable for simulation of tillage equipment in interaction with soil and predicting the soil flow with various deformation patterns.

DEM method predicts the dynamic behavior of soil by solving the equation of motion for the soil-to-soil and soil-to-tool interactions. However, it is only suitable to simulate prescribed tool motions. Most DEM codes have limitations in predicting the dynamic motions of the tool when the soil reaction forces alter with the motion (like in a rotary tiller or a loader bucket). In these applications, the kinematics and kinetics from DEM soil-to-soil and soil-to-tool interactions should be coupled with Multibody Dynamics (MBD) method. MBD can be a proper tool to simulate the dynamics of the tool in the soil-to-tool interaction modeling. Coupling MBD with DEM gives the opportunity to simulate more complex tool motions and accounts this multiphysics modeling in predicting the soil reaction forces on the tool.

It is hypothesized that the DEM-MBD coupling can predict the soil reaction forces in a soil-t-tool interaction application using the discreteness principle in DEM and kinematics of rigid bodies

in MBD. Currently, there are limited quantitative validations of the soil-to-tool interaction using DEM-MBD coupling simulation. These validations are required before this technique can be used in industrial scale applications such as rotary tiller tools and loader buckets.

The overall goal of this research is to develop simple tests for calibration of DEM soil model and validation of the DEM-MBD co-simulation of soil-to-tool interaction. Specifically, the objectives are:

- to characterize soil for DEM calibration and to capture the dynamic soil behaviors from the angle of repose and cone penetrometer tests

- to develop simple soil-to-tool interaction system where the tool is moving in a pendulum motion and measure the soil reaction forces (draft and vertical)

- to quantitatively predict soil reaction forces (draft and vertical) from the soil-to-pendulum interaction using EDEM-LMS Virtual.Lab Motion co-simulation

Following the current introductory chapter, this thesis is organized into four additional chapters. Chapter 2 will review the previous literature and background for the soil-to-tool modeling. Chapter 3 describes the laboratory tests for soil characterization and soil-to-pendulum experiment. It also covers the DEM calibration using cone penetrometer and angle of repose tests and soil-to-pendulum DEM simulation procedures. Chapter 4 presents the results and discussion from DEM soil model calibration and validation for DEM only simulations and DEM-MBD co-simulations in predicting soil reaction forces from the soil-to-pendulum interaction. Finally, Chapter 5 discusses the conclusion and recommendations for future research.

CHAPTER 2.   LITERATURE REVIEW

According to Vilde (2003), tillage is the most expensive and power consuming part of the agriculture process. Therefore, the tillage equipment needs to be as efficient as possible and consume the minimum amount of energy while providing the desirable soil quality for plant growth. Understanding the soil dynamics under load from the tillage equipment is essential for engineers to develop or modify tillage equipment and evaluate productivity.

The most important parameter to evaluate the performance of the tillage equipment is the amount of soil flow and disturbance (Godwin, 2007) which facilitate the flow of air and water through soil to help seed germination and root growth. However, the soil reaction forces under tool load affect the power consumption and should be considered when selecting a tillage tool. According to Godwin (2007), two components of reaction forces are to be studied: horizontal (draft or pull) force which is the amount of force required to push or pull the implement through the soil, and vertical force which is the implement's force assisting or preventing penetration into the soil. In order to optimize the tillage power consumption, the draft force needs to be as small as possible, and vertical force needs to be directed downward to aid in maintaining the tool in the ground. Measuring these soil reaction forces is expensive and time-consuming through prototyping the exact implement or performing field tests. Therefore, using soil-to-tool modeling utilizing empirical, analytical, or numerical methods is preferable to predict the forces.

2.1   Soil modeling

There are different methods to predict the soil dynamics and reaction forces in a soil-tool interaction system. The empirical equations are one of the methods which are derived from observation and experimental data. Another method is the analytical solutions which are based on fundamental laws of physics and are derived using limit equilibrium analysis. More modern methods are

called numerical methods which consist of continuum methods like Finite Element Method (FEM) that assumes the soil as a continuum material, and discrete methods like Discrete Element Method (DEM) that treat the soil as discrete granular material. A brief description of previous works related to soil modeling using these methods are presented in the following sections (Table 2.1).

Table 2.1: Selection of previous works in soil-to-tool interaction modeling

Modeling method	Author(s)	Remarks
Empirical	Larson et al. (1968)	Draft force prediction equation for model molboard plow
	Luth and Wismer (1971)	Horizontal and vertical force prediction equation for inclined blade in sand soil
	Wismer and Luth (1972)	Horizontal and vertical force prediction equation for inclined blade in clay soil
Analytical	Terzaghi (1943)	The first 2D soil failure model for wide blade, based on the passive earth pressure theory
	Osman (1964)	Determined critical soil and tool parameters affecting the soil-tool interaction problems
	Reece (1965)	Fundamental equation to predict draft force
	Hettiaratchi et al. (1966)	Set of charts to determine the N factors presented in Reece (1965) equation
	Soehne (1956)	Used free body diagram to predict draft force for inclined blade
	Payne (1956)	The first 3D soil failure model
	Hettiaratchi and Reece (1967)	3D soil failure model for tines
	Godwin and Spoor (1977)	3D soil failure model for narrow tines
	McKyes and Ali (1977)	3D soil failure model for narrow blades - reevaluated the N factors for 3D models
	Swick and Perumpral (1988)	Dynamic soil failure model - considered effect of too speed on draft force
FEM	Yong and Hanna (1977)	The first 2D FEM model for soil cutting

Table 2.1 – continued

Modeling method	Author(s)	Remarks
	Chi and Kushwaha (1990)	FEM soil failure model for narrow blades - accounted for friction between soil and tool
	Plouffe et al. (1999a)	FEM model for moldboard plow
DEM	Obermayr et al. (2011)	DEM soil model for simple blade in cohesionless materials
	Chen et al. (2013)	DEM soil model for cultivator sweep in agricultural soils
	Tamás et al. (2013)	DEM soil model for cultivator sweep - change in rake angle and speed

2.1.1 Empirical methods

One of the first empirical equations was developed by Larson et al. (1968) to predict the draft force of model moldboard plows in the soil. In this work, a series of physical tests were performed in a soil bin using four different soil types (from sandy loam to silty clay) with various soil moisture contents. Three model moldboard plows with different dimensions were passed though the soil at various speeds. Using the soil bin test data, the empirical equation was developed to predict the draft force as it related to plow width, plow speed, soil bulk density, apparent soil cohesion, soil-to-soil angle of internal friction, and gravitational acceleration. However, the vertical force was not studied in this work.

Luth and Wismer (1971) also developed an empirical equation to predict the horizontal and vertical soil reaction forces for inclined blades working in sand. They performed several tests on a chisel, infinite-width blade, and finite-width blade in soil bin filled with air dry sand at three levels of bulk density. They utilized the dimensionless analysis and statistical curve fitting program to develop the prediction equation of horizontal and vertical soil reaction forces with the standard error of 13% for both forces, respectively. It was also concluded that an upward vertical force is expected from the blades with rake angles greater than 65°. Wismer and Luth (1972) repeated the same procedure for cohesive clay soil to predict the soil reaction forces for the same tool shapes.

They used high plasticity clay with 93% saturation and two levels of compaction (resulting in two levels of soil strength). They were able to provide a prediction equation for horizontal and vertical forces with 20% and 24% standard error, respectively.

The empirical-based prediction equations require a large number of physical experiments and database which can be relatively expensive and time consuming. They are limited to a specific tool geometry and working condition, although they can be useful for deriving prediction equation for more complex geometry as in Larson et al. (1968). For these reasons, analytical methods are an alternative approach to predict the soil reaction forces.

2.1.2 Analytical methods

The soil cutting model was first introduced by Terzaghi (1943) for a two-dimensional soil failure in contact with a wide blade, based on the passive earth pressure theory. In this theory, the failure zone consists of two zones: 1) a passive Rankine zone (Rankine, 1857) which has an angle of $45° - \phi/2$ to the horizontal (where ϕ is the soil-to-soil angle of internal friction), and 2) a logarithmic spiral curve which is the lower boundary of the soil failure.

Osman (1964) determined the soil and tool parameters that affect the earth-moving problems by using dimensionless analysis. He stated that the soil and tool parameters affecting the draft force (F) are: soil cohesion (c), soil-to-soil angle of internal friction (ϕ), soil density (γ), soil-to-tool adhesion (c_a), soil-to-tool angle of friction (δ), rake angle (θ), surcharge pressure (q), and cutting depth (z). Based on these parameters, Reece (1965) introduced a fundamental equation for solving the earth-moving problems as expressed in Equation 2.1. In this equation, the N factors are dimensionless numbers which represent the shape of the soil failure zone. Hettiaratchi et al. (1966) provided a set of charts to determine these N factors based on the soil-to-soil angle of internal friction, the soil-to-tool angle of friction, and rake angle.

$$F = czN_c + \gamma z^2 N_\gamma + qbN_q + c_abN_a \qquad (2.1)$$

Soehne (1956) (Gill and Berg, 1968) also proposed a two-dimensional soil failure model for a simple inclined blade. He used the free body diagram of all the forces applied on a block of soil in

contact with the tool and utilized the equilibrium equations to propose a prediction equation for draft force. This equation related the draft force to the weight of soil segment, soil cohesion, soil-to-soil and soil-to-tool angle of friction, angle and area of forward shear failure surface, rake angle, and soil acceleration force. To verify the prediction equation, Soehne (1956) performed experimental tests with an inclined tool in loam soil which showed 18% over-prediction of draft force calculated from the equation compared to experimentally measured one.

The first three-dimensional soil failure model was introduced by Payne (1956). He performed a series of field and laboratory tests and observed that the top surface soil heave during the tillage. Based on these observations, he proposed a soil failure zone comprised of a triangular center wedge, a center crescent, and two side blocks. He also concluded that the radial dimensions of the heave can be predicted from the soil cohesion, soil-to-soil angle of internal friction, soil-to-tool adhesion and angle of friction.

Additionally to the two-dimensional models, Hettiaratchi and Reece (1967) developed a three-dimensional soil failure model for tines. This model consisted of the forward failure, which is in front of the tool, and the sideways failure, which represents the horizontal displacement of soil sideways and backward of the tool. The forward failure force acts at an angle of soil-to-tool friction (δ) to the interface and is calculated from Equation 2.1. The sideways failure force acts normal to the interface and is determined by O'callaghan-Farrelly (1964) and also accounts for the gravitational component. However, this theory showed over-prediction of the draft force for smaller values of the aspect ratio (the ratio of the depth of the tine over the width of it) in their experiment of moving a rigid tine through sand at different depth and rake angles.

Godwin and Spoor (1977) proposed a new soil failure model for narrow tine based on critical depth. The model composed of two sections: 1) the lateral failure below the critical depth, where displaced soil has forward and sideways components, and 2) the crescent failure above the critical depth, where displaced soil has forward, sideways and upward components. The lateral failure was similar to Hettiaratchi and Reece (1967), and the crescent section itself was comprised of a linear section ahead of the tine with the same width as the tine and two curved sections of a

constant radius at the sides. The linear portion force was determined from Equation 2.1, and the side sections forces were derived from solving the two-dimensional theory for a small element and integrating across the whole side crescent sections.

McKyes and Ali (1977) suggested a similar three-dimensional soil failure model for the narrow blades. Their model, similar to Godwin and Spoor (1977), consisted of a center wedge with the same width as the blade and two side crescents. However, instead of using the logarithm spiral failure boundary at the tip of the blade, McKyes and Ali (1977) assumed a straight line which formed an unknown angle (β) to horizontal. In this approach, they solved the model by applying the mechanics of the equilibrium directly. The center section force was determined from the two-dimensional theory, and the crescent section force was analyzed by integrating across the whole section. The proposed equation for predicting the draft force was similar to Equation 2.1, however, the N factors N_γ, N_c and N_q were reevaluated for three-dimensional failure to $N_{\gamma H}$, N_{cH} and N_{qH}. These factors were functions of forward rupture distance, rupture angle (β), depth, rake angle, soil-to-soil angle of internal friction, soil-to-tool angle of friction, and the aspect ratio. β was determined by minimizing the $N_{\gamma H}$ by trial and error. Further, Mckyes (1985) provided a set of charts for determining these new N factors for certain values of soil-to-soil angle of internal friction (ϕ) and soil-to-tool angle of friction (δ).

All models that have been described so far were static or quasi-static models and were only suitable for slow-moving tools. Swick and Perumpral (1988) proposed a dynamic soil failure model which considered the effect of the tool speed. In this approach, the soil failure zone was similar to McKyes and Ali (1977) model with a center wedge and two side crescents with a straight line at the lower boundary. However, Swick and Perumpral (1988) proposed a new internal angle to determine the outer points of the side sections where McKyes and Ali (1977) assumed these points were vertically aligned with the tip of the tool. The force calculation was similar to McKyes and Ali (1977) with the addition of the acceleration force.

The analytical methods have been relatively accurate to predict the soil reaction forces, but they are limited to simple tool geometry and the soil was assumed as a continuum and not of granular

material. This assumption causes an inaccurate prediction of the soil flow and deformation. The development in the powerful computers with high running speed and memory, along with recent advances in physics-based soil model and dynamic soil behavior presented a new opportunities of using the numerical methods for modeling the soil-tool interaction and predicting the soil reaction forces.

2.1.3   Numerical methods

The Finite Element Method (FEM) is one of the numerical methods which is able to analyze the complex engineering problems, such as ones including geometric and material nonlinearities (Upadhyaya et al., 2002). The FEM has been widely used in agricultural industry, for solving the soil related problems such as soil compaction by Chi et al. (1993), Raper and Erbach (1990), and Liu and Wong (1996), soil traction by Hu and Abeels (1994) and Nakashima and Wongt (1993), and soil-to-tool interaction problems.

Yong and Hanna (1977) proposed, for the first time, a two-dimensional FEM model for soil cutting. The FEM model was developed for a continuous cutting of the clay soil at the tip of the blade in which the soil performance and soil reaction forces under the action of a cutting blade were studied. By performing an experiment with a cutting blade moving with a constant speed through the compacted clay soil, they showed good agreement between the predicted horizontal force from FEM and measured one from experiment. Chi and Kushwaha (1990) developed a FEM model using Duncan and Chang (1970) hyperbolic stress-strain model to study the soil failure under a narrow blade. In addition to accounting for progressive and continuous cutting (similar to Yong and Hanna (1977)), the friction between the soil and the tillage tool was also taken into account. The soil reaction forces were determined both in the FEM analysis and a soil bin test with same tool geometry. The predicted horizontal (draft) forces were in agreement with ones measured in the soil bin tests. However, there was a slightly over-prediction in the magnitude of vertical forces.

Plouffe et al. (1999b) analyzed a more complex geometry of tillage tool and used FEM to simulate the moldboard plow at different depth and speed in clay soil. They also performed soil bin

and field experiment to validate their FEM model. The predicted soil horizontal reaction forces were in good agreement with the field experiment, however, the predicted vertical forces were lower than measured ones for speeds lower than 1 m/s. In further FEM analysis and field experiments with moldboard plow, Plouffe et al. (1999a) stated that other numerical methods should be combined with FEM to capture the overall behavior of the tool and not just an isolated section of it.

Another numerical method which is widely used to simulate soil and other granular material is Discrete Element Method (DEM), which unlike FEM considers the granular material as discrete individual particles. This method was introduced by Cundall and Strack (1979), however based on O'Sullivan (2011), the first three-dimensional DEM was used in 2002.

Obermayr et al. (2011) used DEM to model the soil-to-tool interaction and predicted the draft forces in a cohesionless soil. They used triaxial test as a calibration, and an experimental test for validation, in which a single vertical blade was moved through two types of material (steel balls, round gravel) with a constant velocity. Their model showed a good agreement with the experiment. However, agricultural soil is cohesive and some tillage tools have more complicated shapes. Chen et al. (2013) developed a DEM model to simulate soil-to-sweep interaction in three different soil types including coarse sand and sandy loam. They calibrated the stiffness of the particles in their model with soil cutting forces from an experimental data and then validated the simulation using the soil disturbance from those three soils. Their model predicted the soil disturbance characteristics with 10% error. Tamás et al. (2013) used DEM for modeling soil-to-sweep interaction and prediction of the draft forces and soil loosening process based on the change in rake angle and tool speed. They also used Computer-aided Design system (CAD) to import the complicated geometry of the sweep into the DEM. Their model provided good match in the draft force between simulation and the experimental result of a soil bin with 4-15% error. They further refined their DEM model parameters using a virtual DEM triaxial test and decreased the error to 4-9%. They concluded that DEM is an effective tool to calculate the draft force for non-homogeneous unsaturated soil.

2.2   Discrete Element Method (DEM)

The Discrete Element Method (DEM) is a numerical method introduced by Cundall and Strack (1979) to determine the dynamic behavior of granular materials. This method considers the individual particles in the granular system and their interaction, unlike the continuum models where the system is assumed to behave as a continuous material and the relative movements and the rotation of each particles within the system is neglected (O'Sullivan, 2011).

O'Sullivan (2011) mentioned two main reasons to use DEM in both academic and industry level. First, loads and deformations can be applied to virtual samples to model the dynamic behavior of the granular material in the physical tests. This method facilitates the analysis of the contact forces between the particles, the particles' rotation, and the particle and contact orientation, which would be impossible to achieve with laboratory experiments. Second, the analysis of systems with large-displacement of the granular material is possible with DEM model whereas it is challenging to do so in continuum approaches such as FEM. The example of these types of mechanism in the agricultural concept is the soil cutting equipment and the prediction of the soil flow during the tillage process.

In DEM, the particles are "soft particles" which unlike the name are rigid but can overlap at the contact point. Based on Cundall and Strack (1979), this overlap is small in comparison with the particle size and the magnitude of the overlap is related to the contact force as represented in Equation 2.2

$$F_n = K_n \delta_n \tag{2.2}$$

where F_n is the contact normal force, K_n is the normal stiffness, and δ_n is the overlap at the contact point.

Cundall and Strack (1979) stated that in DEM, the contact forces between two particles and the resultant motion of each particle after the contact are calculated based on equation of motion. It is assumed that in the time step in which the forces are calculated, the velocities and accelerations of the particles are constant. In addition, the time step is small enough so that during a single time step only the immediate neighbors to the particle have an influence on the contact forces. In each

time step, the motion of the particle resultant from the contact force is calculated by the Newton's second law, and the displacement of the particle resultant from the contact forces is determined from the force-displacement law.

The work flow of the sequence of calculation in the DEM simulation is shown in Figure 2.1. To implement DEM simulation, first, the geometry, the material properties, and the system loading or deformation schedule are defined. Then the simulation starts as a transient or dynamic analysis for a specified number of iterations. At each time step, the contacting particles are defined, and the inter-contact forces between them are calculated. The forces and torques acting on each particle are then calculated based on these inter-contact forces which determine the translational and rotational movement of the particles respectively. The displacement and orientation of the particles are updated, and at the next time step, the contact forces are calculated based on these updates. The process is repeated until the simulation reaches the specified number of iterations.

2.2.1   DEM contact models

As represented in Figure 2.1, the first action in each time step of the DEM simulation is to find the contacting particles. This stage is called *contact detection* (Hogue, 1998) which is described as a series of calculation on developing an algorithm to find the particles that are in contact or are likely to come in contact in a given time increment and create a "neighbor list". Then the contact forces are calculated only for the particle pairs inside this "neighbor list".

The inter-particle contact forces are divided into two components, normal and tangential to the contact point. These normal and tangential components are represented by models which consist of a combinations of springs, slides and dampers and are called *contact models*. The simplest contact model for the normal component is proposed by Hertz (1882) and for the tangential component is developed by Mindlin (1949) and Mindlin and Deresiewicz (1953). These contact models along with some more complex ones are described below.
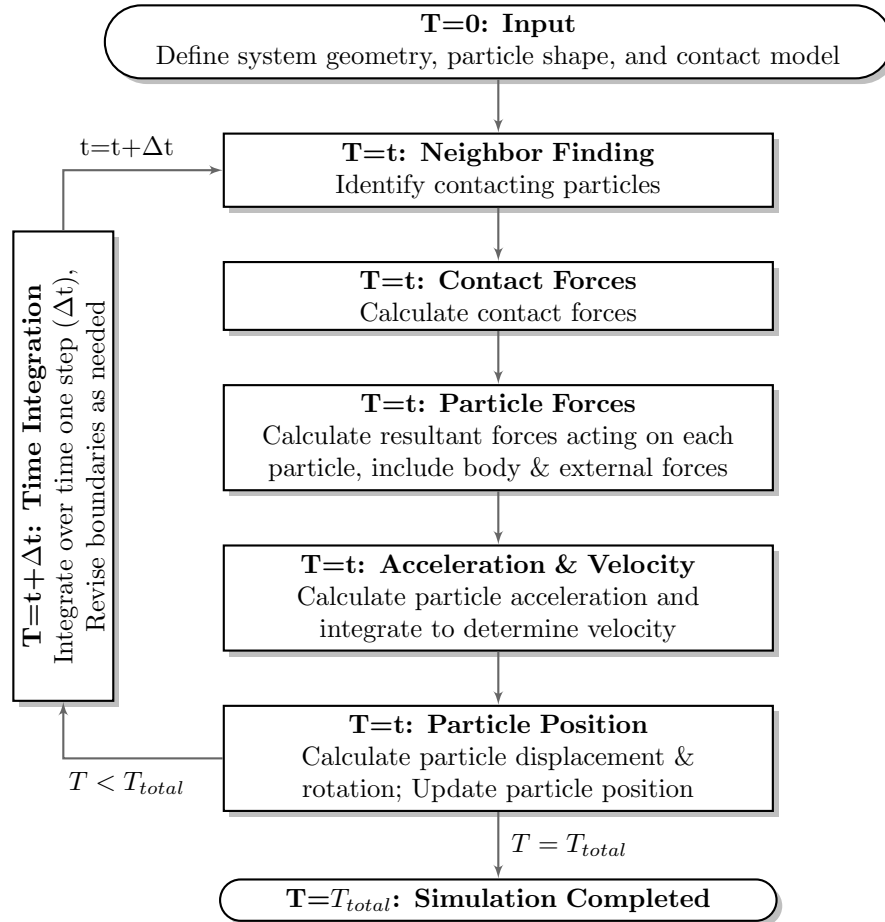
Figure 2.1: Schematic diagram of sequence of calculation in a DEM simulation (O'Sullivan, 2011)

2.2.1.1 Hertzian normal contact model

The Hertzian theory (Hertz, 1882) is used to determine the normal component of the inter-particle contact forces. This theory is based on the linear elasticity of the contacting spheres where there is an initial point contact between the two particles and it will grow into a contact area while the particles undergo surface traction and deformation. Other assumptions of this theory are that the surface of the particles are smooth, the contact area is small compared to the particle size, and there are no other interactions between the particles outside of the loading area.

Based on the Hertzian theory (DEM Solutions Ltd, 2014) the normal contact force (F_n) between the two contacting spheres is calculated as

$$F_n = \frac{4}{3}E^*\sqrt{R^*}\delta_n^{\frac{3}{2}} \tag{2.3}$$

where δ_n is the overlap between the two spheres and E^* and R^* are the effective Young's modulus and effective particle radius respectively and are calculated as follows

$$\frac{1}{E^*} = \frac{1 - \nu_{s_1}^2}{E_{s_1}} + \frac{1 - \nu_{s_2}^2}{E_{s_2}} \tag{2.4}$$

$$\frac{1}{R^*} = \frac{1}{R_{s_1}} + \frac{1}{R_{s_2}} \tag{2.5}$$

where ν_{s_1} and ν_{s_2} are the Poisson's ratio, E_{s_1} and E_{s_2} are the Young's moduli, and R_{s_1} and R_{s_2} are the sphere radii for the spheres s_1 and s_2, respectively.

2.2.1.2 Mindlin-Deresiewicz tangential contact model

The Mindlin-Deresiewicz theory developed by Mindlin (1949) and Mindlin and Deresiewicz (1953) is the main part of most of the contact models used in DEM simulations (DEM Solutions Ltd, 2014). The main assumption of this theory is that the tangential traction does not influence the normal traction distribution, which is calculated based on the Hertizan theory. Mindlin (1949) showed that when the normal force is constant, by applying the tangential force, there is a "slip" on some part of the contact area and a "stick" on the other parts. As the contact area is circular, based on Hertzian theory, the "sticking" area is in the central circle, whereas the slip occurs in an annular region around the "sticking" area. The work of Mindlin and Deresiewicz (1953) indicates that the tangential stiffness of the tangential contact spring depends on the current normal load, the current tangential load, the load history, and whether the tangential load is increasing or decreasing.

As stated in O'Sullivan (2011) the laws of friction give the relationship between the normal and tangential traction as follows.

$$f_t(r) = \mu f_n(r) \tag{2.6}$$

where r is the distance from the center of the contact circle ($0 \leq r \leq a$ where a is the contact radius) and f_n and f_t are the normal and tangential traction, respectively. At the initial tangential

loading, it is assumed that the normal force is applied first and is constant, and the tangential force increases monotonically. If the radius of the sticking area is b and the radius of the total contact circle is a, the tangential traction at a distance r from the center of the contact circle is obtained from

$$f_t(r) = \frac{3\mu F_n}{2\pi a^3}\sqrt{a^2 - r^2} \qquad\qquad b \leq r \leq a \qquad (2.7)$$

$$f_t(r) = \frac{3\mu F_n}{2\pi a^3}\left(\sqrt{a^2 - r^2} - \sqrt{b^2 - r^2}\right) \qquad\qquad 0 \leq r \leq b \qquad (2.8)$$

The tangential force is given by

$$F_t = 2\pi \int_0^a f_t(r)r\,dr = \mu F_n\left(1 - \frac{b^3}{a^3}\right) \qquad (2.9)$$

The relative tangential displacement of two contacting spheres is given by Mindlin (1949) as

$$\delta_t = \frac{3\mu F_n}{16G^* a}\left(1 - \frac{b^2}{a^2}\right) \qquad (2.10)$$

where G^* is the effective shear modulus and calculated as

$$\frac{1}{G^*} = \frac{2 - v_{s_1}}{G_{s_1}} + \frac{2 - v_{s_2}}{G_{s_2}} \qquad (2.11)$$

where G_{s_1} and G_{s_2} are the shear moduli of the spheres s_1 and s_2 respectively.

The process of slip is irreversible, meaning that when the loading is reversed the slip area will not decrease. Instead, a region called "counter-slip" will start forming at the edge of the contact. So in this case, the contact area is divide into three sections: no slip area, slip area, and counter-slip area. Now the tangential traction along the contact surface is determine by the following equations

$$f_t(r) = \frac{3\mu F_n}{2\pi a^3}\sqrt{a^2 - r^2} \qquad\qquad c \leq r \leq a \qquad (2.12)$$

$$f_t(r) = \frac{3\mu F_n}{2\pi a^3}\left(\sqrt{a^2 - r^2} - 2\sqrt{c^2 - r^2}\right) \qquad\qquad b \leq r \leq c \qquad (2.13)$$

$$f_t(r) = \frac{3\mu F_n}{2\pi a^3}\left(\sqrt{a^2 - r^2} - 2\sqrt{c^2 - r^2} + \sqrt{b^2 - r^2}\right) \qquad\qquad 0 \leq r \leq b \qquad (2.14)$$

Then the tangential force is derived by the integration of Equations 2.12 through 2.14 over the entire particle radius, which gives the following equation

$$F_t = \mu F_n\left[1 - \left(\frac{b}{a}\right)^3\right] - 2\mu F_n\left(\frac{c}{a}\right)^3 \qquad (2.15)$$

As stated in O'Sullivan (2011) the granular material response is mainly related to the normal force and the tangential force can be simplified to facilitate the calculation in the DEM contact models. Therefore, in some DEM simulations (eg. DEM Solutions Ltd (2014)) the tangential force is only related to the tangential overlap (δ_t) and the tangential stiffness (S_t), and the complicated tangential stress distribution (Equation 2.15) is simplified. In this case, the tangential force is formulated as

$$F_t = S_t \delta_t \tag{2.16}$$

with

$$S_t = 8G^* \sqrt{R^* \delta_n} \tag{2.17}$$

where R^* and G^* are the effective radius and shear modulus which are derived from Equations 2.5 and 2.11 respectively.

2.2.1.3 Normal and tangential damping models

Both normal and tangential forces have damping components. The normal damping force ($F_n{}^d$) is calculated as (DEM Solutions Ltd, 2014)

$$F_n{}^d = -2\sqrt{\frac{5}{6}}\beta\sqrt{S_n m^*}v_n{}^{rel} \tag{2.18}$$

where $v_n{}^{rel}$ is the normal component of the relative velocity, m^* is the equivalent mass, and S_n is the normal stiffness. m^*, S_n, and β are determined from the following equations.

$$\frac{1}{m^*} = \frac{1}{m_{s_1}} + \frac{1}{m_{s_2}} \tag{2.19}$$

$$S_n = 2E^* \sqrt{R^* \delta_n} \tag{2.20}$$

$$\beta = \frac{\ln e}{\sqrt{\ln^2 e + \pi^2}} \tag{2.21}$$

where m_{s_1} and m_{s_2} are the mass of sphere s_1 and s_2 respectively, and e is the coefficient of restitution (Tsuji et al., 1992).

According to DEM Solutions Ltd (2014), the tangential damping force ($F_t{}^d$) is formulated as

$$F_t{}^d = -2\sqrt{\frac{5}{6}}\beta\sqrt{S_t m^*}v_t{}^{rel} \tag{2.22}$$

where $v_t{}^{rel}$ is the tangential component of the relative velocity, and S_t is the tangential stiffness which is calculated from Equation 2.17.

2.2.1.4 Rolling friction model

In the original DEM code developed by Cundall and Strack (1979), the particles were assumed to be smooth spherical particles. However, Sakaguchi et al. (1993) modeled the discharge of acrylic rods through a silo with basic DEM and proved that the DEM particles were easier to roll compared to the actual ones. Therefore, they introduced a new rolling resistance model which adds a resistance to particle's rotation at the contact point. In their model, the resisting moment (M_{rf}) and the rolling friction (τ_i) are calculated based on the following equations.

$$M_{rf} = \mu_r F_n \tag{2.23}$$

$$\tau_i = \mu_r F_n R_i \omega_i \tag{2.24}$$

where μ_r is the coefficient of rolling friction, R_i is the distance of the contact point from the center of a mass, and ω_i is the unit angular velocity vector of the particle at the contact point.

2.2.1.5 Parallel bond model

Potyondy and Cundall (2004) first presented the parallel bond model to simulate the cemented behavior of rock. This contact model can be used to bond the particles together using a finite-size "glue" bond (DEM Solutions Ltd, 2014) where it can break only when the forces exceed the maximum normal and/or tangential critical shear stress. When a parallel bond is not present at the contact, the equations from Hertzian and Mindlin contact models govern on the particles. Based on Potyondy and Cundall (2004), the parallel bond model is described by five model parameters: normal stiffness per unit area $(\bar{k}^n)$, shear stiffness per unit area $(\bar{k}^s)$, critical normal stress $(\bar{\sigma}_c)$,

critical shear stress ($\bar{\tau}_c$), and bond radius ($\bar{R}$), and are assigned as

$$\bar{k}^n = \frac{\bar{E}_c}{R_{s_1} + R_{s_2}} \tag{2.25}$$

$$\bar{k}^s = \frac{\bar{k}^n}{\frac{\bar{k}^n}{\bar{k}^s}} \tag{2.26}$$

$$\bar{R} = \bar{\lambda} min(R_{s_1}, R_{s_2}) \tag{2.27}$$

where $\bar{E}_c$ is the bond Young's modulus, R_{s_1} and R_{s_2} are the sphere's radii for the sphere s_1 and s_1 respectively, and $\bar{\lambda}$ is the bond-radius multiplier.

The total force ($\bar{F}_i$) and moments ($\bar{M}_i$) of the parallel bond are calculated as

$$\bar{F}_i = \bar{F}_n + \bar{F}_t \tag{2.28}$$

$$\bar{M}_i = \bar{M}_n + \bar{M}_t \tag{2.29}$$

where $\bar{F}_n$, $\bar{M}_n$ and $\bar{F}_t$, $\bar{M}_t$ denote the normal and tangential forces and moments, respectively. When the parallel bond model initially forms between the adjacent spheres, the $\bar{F}_i$ and $\bar{F}_i$ are both zero. These forces and moments are adjusted incrementally each time step according to

$$\delta \bar{F}_n = \bar{k}^n A \delta_n \tag{2.30}$$

$$\delta \bar{F}_t = \bar{k}^s A \delta_t \tag{2.31}$$

$$\delta \bar{M}_n = \bar{k}^s J \Delta \theta_n \tag{2.32}$$

$$\delta \bar{M}_t = \bar{k}^n I \Delta \theta_t \tag{2.33}$$

where A, I and J are the area, moment of inertia and polar moment of inertia of the parallel bond cross section respectively, and are calculated as

$$A = \pi \bar{R}^2 \tag{2.34}$$

$$I = \frac{\pi}{4} \bar{R}^4 \tag{2.35}$$

$$J = \frac{\pi}{2} \bar{R}^4 \tag{2.36}$$

The maximum normal and shear stresses acting on the parallel bond are formulated as

$$\bar{\sigma}_{max} = \frac{-\bar{F}_n}{A} + \frac{|\bar{M}_t|\bar{R}}{I} \tag{2.37}$$

$$\bar{\tau}_{max} = \frac{|\bar{F}_t|}{A} + \frac{|\bar{M}_n|\bar{R}}{J} \tag{2.38}$$

.

If the maximum normal stress exceed the normal strength ($\bar{\sigma}_{max} \geq \bar{\sigma}_c$) or the maximum shear stress exceeds the shear strength ($\bar{\tau}_{max} \geq \bar{\tau}_c$), the parallel bond breaks.

2.2.2 DEM input parameters determination

Depending on which contact model is used for the DEM simulation, there are material input parameters that need to be determined so the model can be simulated correctly. For a basic Hertz-Mindlin contact model, the DEM input parameters are listed as: material properties including Poisson's ratio, solid density, and shear modulus; interaction properties including coefficient of restitution, coefficient of static friction, and coefficient of rolling friction; particle shape and size; and time step (DEM Solutions Ltd, 2014). If the parallel bond model is also used in the simulation, additional input parameters are added to the list including: normal and shear stiffness per unit area, critical normal and shear stress, and bonded disk radius which are described in Section 2.2.1.5. There are few ways to determine these parameters including direct measurements, calibration and estimation from literature.

2.2.2.1 Direct measurement of DEM input parameters

The particle shape and size of the granular material modeled in DEM are among the few DEM parameters that can be measured in the laboratory. Particle shape can be characterized by sphericity and aspect ratio. Sphericity (ξ) expresses shape attribute of a particle relative to that of a sphere for the equivalent volume and formulated as (Chancellor, 1994)

$$\xi = \frac{d_e}{d_c} \tag{2.39}$$

where d_e is the diameter of a sphere of the same volume as the particle and d_c is the diameter of the smallest circumscribing sphere or the longest diameter of the object. Aspect ratio is usually defined by the ratio of the minor axis (the smallest dimension) by the major axis (the largest dimension) of the particle.

Solid density of granular material can also be determined by dividing the particle mass by the particle volume. As González-Montellano et al. (2012) and Höhner and Wirtz (2012) used in their work, the mass of the particle can be directly measured using a precision balance and the volume of the particle can be measured based on the ASTM International (2014) method where the particles are submerged in water.

Young's modulus defines the relationship between the stress and strain in an elastic portion of the uniaxial deformation of a material. González-Montellano et al. (2012) and Wang et al. (2015) used the compression test to measure the Young's modulus of corn. In this method, the specimen was loaded in a uni-axial compression test and the force-deformation curve was produced to estimate the Young's modulus. Individual particle uniaxial compression test, however, is impossible to do with soil particles (less than 2 mm).

Coefficient of restitution is another DEM input parameter that can be measured. Wang et al. (2015) used a high speed camera to measure the particle-geometry coefficient of restitution for corn. They freely dropped corn grains from certain height onto the horizontal surface and used the high speed camera to capture the velocity of the grain before and after the impact. Chou et al. (2012) also used the same procedure to measure the particle-to-geometry and particle-to-particle coefficient of restitution.

A few studies have been done to measure the sliding friction coefficient. Li et al. (2005) modelled glass and steel particles and measured the sliding friction by gluing the particles to an upside down container over a horizontal plane made with the same material (for particle-particle) or the opposite material (for particle-geometry) and applying shear force to slide the particles. Chen et al. (2015) used the same method to measure the particle-to-particle sliding friction for glass particles on a glass plane.

2.2.2.2 Calibration of DEM input parameters

Some of the DEM input parameters are challenging to measure in-situ or in laboratory, especially for the smaller particle sizes. In this case, bulk calibration of the parameters is needed to find an accurate set of values. Based on Coetzee (2016), in this approach, a specific material bulk property is measured either in-situ or in laboratory. Then, the exact experiment setup is numerically modeled by following the field or laboratory setup and procedure. The DEM input parameters are then changed to obtain the bulk responses of the simulation as close as possible to the measured values. The key element in this method is that the calibration experiment should be different from the final application, or the results would only be a sensitivity analysis and does not have any benefit in designing a new system (Coetzee (2017)).

Coefficient of sliding and rolling friction are among those input parameters that are challenging to measure and studies have been done to calibrate these coefficients (Mousaviraad et al., 2017; Tekeste et al., 2018). Static and dynamic angle of repose and the hopper discharge tests are widely used to calibrate the sliding and rolling frictions. Combarros et al. (2014) performed both the dynamic angle of repose using a rotating drum and the static angle of repose using a hollow cylinder filled with spheres made of aluminum oxide and pulling it upward to form a pile on a flat surface. Then, the experiments were modeled to obtain the optimum values for rolling friction, particle-particle sliding friction and the coefficient of restitution. To calibrate the particle-particle sliding and rolling friction, Derakhshani et al. (2015) facilitated only the static angle of repose experiment using a rectangular container filled with sand with one sliding door to let the material flow. They measured the angle of repose and the time for the material to completely discharge from the container. The model was validated with 4% error, however, they used the hollow cylindrical angle of repose as their validation application which was very similar to the calibration experiment. Li et al. (2013) used the very similar process to calibrate the particle-particle sliding and rolling friction for soy beans and yellow rice. They filled a hopper with the material and by discharging it a pile formed on the horizontal ground underneath. Static angle of repose and discharge time were

measured. The model was successfully validated by modelling a charging process of a shaft furnace and predicting the particle flow with and burden profile.

The penetration test is another known experiment for calibration of DEM input parameters. In this test, a tool with different shapes (like cones, flat plates, or angled wedges) inserted into the material to measure the friction parameters. Asaf et al. (2007) proposed an in-situ calibration procedure utilizing the penetration test with three different penetration tools (flat plate, 30° wedge, and 90° wedge) to calibrate the particle-to-particle friction coefficient and particle stiffness. The force versus displacement curves were obtained from both the physical and DEM experiment. An optimization algorithm was employed to minimize the area difference between test and simulation, and the set of accurate values were determined. Ucgul et al. (2014) used the penetration test (with circular disk and 30° cone) to calibrate the particle-particle coefficients of sliding and rolling friction in cohesionless sand.

Some standard laboratory test like triaxial and direct shear tests can also be utilized for bulk calibration of DEM parameters. For instance, Belheine et al. (2009) proposed a calibration procedure using the triaxial test. There were three steps to this procedure: the normal contact stiffness and stiffness ratio (ratio of shear stiffness to normal stiffness) were varied to match the measured values of Young's modulus and Poisson's ratio; the coefficient of sliding friction was adjusted to match the measured dilatancy curve of real material; the coefficient of rolling friction was adjusted to match the stress-strain curve. Coetzee and Els (2009) used direct shear test to calibrate the friction coefficients and particle stiffness for corn. It was concluded that the direct shear test is dependant on both of these parameters.

CHAPTER 3.   MATERIALS AND METHODS

3.1   Soil Characterization

Soil used in current work originated from the Iowa State University Farm located in Boone county in Iowa state. The USDA soil classification was performed for this soil by using the sieve analysis (ASTM International, 2017b) and sedimentation (hydrometer) analysis (ASTM International, 2017a). The result of the soil classification is presented in Table 3.1. Several material characterization tests were performed on the soil to represent its mechanical properties in DEM soil model. Some of these properties can be measured directly from standard laboratory tests including the Atterberg limit tests (plastic and liquid limit), the particle size distribution, the proctor compaction test, the direct shear test, and the triaxial test. Other properties need to be calibrated using virtual design of experiment (DOE) calibration approach. In this approach, the mechanical properties are determined from numbers of simulations and compared to the experiments to find the best DEM input parameters. The laboratory tests performed for the DEM calibration are the angle of repose test, and the cone penetrometer test. An overview of these tests and their purpose in establishing a DEM soil model is shown in Figure 3.1.

Table 3.1: USDA soil classification of the soil sampled from the Iowa State University Farm, Boone, Iowa

% Sand (2-0.05 mm)	% Silt (0.05-0.0002 mm)	% Clay ($<$0.002 mm)	Texture
33.29	45.21	21.50	Loam

In addition, the organic matter of the soil was measured to be 7.1% based on ASTM International (2001a) method, and the soil pH level was determined to be 6.5 using the ASTM International (2001b) method.

25

Figure 3.1: Overview of soil characterization and calibration applications

3.1.1 Atterberg limits and plasticity index

ASTM International (2010) was used to determine the Atterberg limits (liquid and plastic limit) and plasticity index of soil. For the liquid limit (LL) test, a Humboldt hand-operated liquid limit device was used which consisted of a small cup that was dropped from a height of 10 mm. The cup was filled with moist soil sieved with 0.25 mm screen and squeezed down to form a horizontal surface. A groove was formed in the soil using a flat grooving tool. Then the cup was lifted and dropped a few times by turning the crank until two part of the soil came together for about 13 mm along the groove, as shown in Figure 3.2a. The number of drops and the soil moisture content (dry basis, %) of the soil was recorded. The test was repeated three times, and each time the soil was prepared in a way to close the groove in 20, 25, and 30 drops, according to ASTM International (2010). The soil moisture content and the corresponding number of drops was plotted in a semi-logarithmic graph, with soil moisture content on the y-axis and the number of drops in x-axis in logarithmic scale. Linear regression was performed for these points, and the corresponding moisture content for the 25 number of drops was found and reported as the liquid limit.

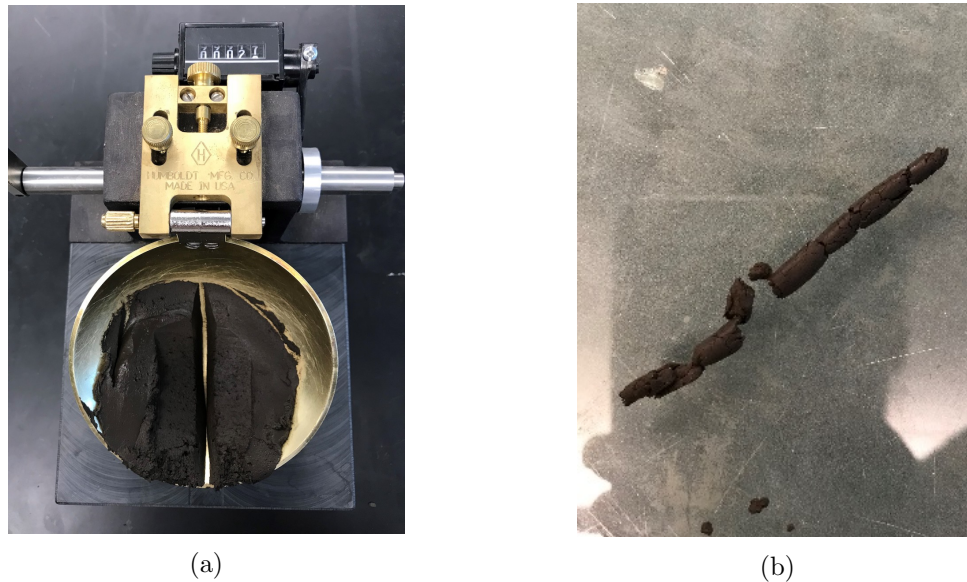(a)   (b)

Figure 3.2: a) Liquid limit test apparatus with two parts of loam soil came together for 13 mm and b) plastic limit test when loam soil was crumbled

To perform the plastic limit (PL) test, the hand method was chosen from the ASTM International (2010). In this method, the 0.25 mm sieved soil is mixed with water to a level which it can be rolled by hand. Small specimen (1.5 to 2 grams) of the moist soil was taken and rolled between finger and a glass plate to reach a 3 mm thread. This procedure did not take more than 2 minutes. Then the thread was kneaded between two hands and rolled again. The procedure was repeated until the soil was crumbled and could no longer be rolled to a 3 mm thread, as shown in Figure 3.2b. The moisture content of the soil was measured at this level and was reported as the plastic limit. The plasticity index (PI) was calculated using the equation PI = LL - PL. The Atterberg limits and plasticity index are shown in Table 3.2.

Table 3.2: Atterberg limits based on soil moisture content (d.b, %) and plasticity index

Liquid limit	Plastic limit	Plasticity index
31.6	24.7	6.9

3.1.2 Particle size distribution

ASTM International (2017b) was used to determine the particle size distribution of the coarse-grained range (0.075 mm to 12.5 mm) of the loam soil using the sieve analysis. For the sieving process, ten U.S.A standard sieves with 200 mm diameter and 50 mm height were selected. These sieves include 12.5 mm, 6.3 mm, 4.75 mm (No.4), 2.00 mm (No.10), 0.85 mm (No.20), 0.50 mm (No.35), 0.25 mm (No.60), 0.15 mm (No.100), 0.106 mm (No.140), and 0.075 mm (No.200). The sieves were stacked on a Humboldt mechanical sieve shaker in descending size moving down. There were also a pan and a cover at the bottom and the top of the sieves, respectively.

The mass of 500 grams of air-dried loam soil (3% moisture content (d.b.)) was carefully poured over the biggest sieve, and the sieves were shaken on the shaker for 10 minutes (ASTM International, 2017b). Then, the mass of soil retained on each sieve was carefully measured and the cumulative

mass retained on each sieve was calculated by adding the mass of soil retained on the Nth sieve and those above it. The percent passing for each sieve is calculated using the following equation.

$$PP_N = 100 \times (1 - \frac{CMR_N}{M_d})$$ (3.1)

where PP_N is the percent passing the Nth sieve, CMR_N is the cumulative mass retained on the Nth sieve in grams, and M_d is the dry mass of the specimen in grams. The graphical presentation is a plot of percent passing versus log of particle size (diameter), as shown in Figure 3.3.

From Figure 3.3 the values of d_{10}, d_{30}, d_{50} and d_{60} were determined which are the particle diameter at which 10%, 30%, 50% and 60% of the soil mass is comprised of particles with a diameter less than these value. The coefficient of uniformity (C_u) and the coefficient of curvature (C_c) were calculated from Equations 3.2 and 3.3 (Craig, 2004). All these values are shown in Table 3.3.
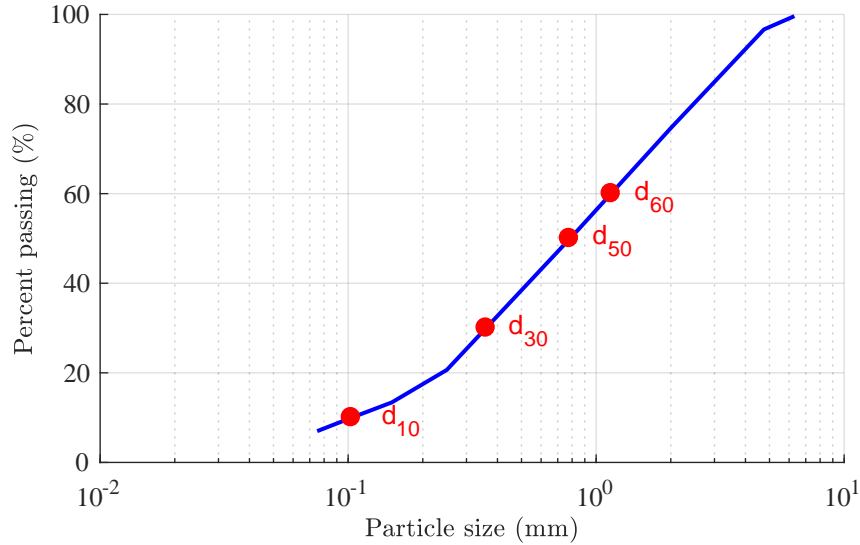

Figure 3.3: Particle size distribution of loam soil from Boon county, Iowa

$$C_u = \frac{d_{60}}{d_{10}}$$ (3.2)

$$C_c = \frac{(d_{30})^2}{d_{60} \times d_{10}} \tag{3.3}$$

Table 3.3: The distribution shape coefficient

Particle diameter (mm)				Coefficients	
d_{10}	d_{30}	d_{50}	d_{60}	C_u	C_c
0.1	0.24	0.78	1.1	11	0.52

3.1.3 Proctor compaction test

ASTM International (2012) standard was used to perform the proctor compaction test on the loam soil and measure the laboratory compaction characteristics of the soil using standard effort was used. In this method, six levels of soil moisture content (d.b.) were selected which were 10%, 12%, 14%, 16%, 18% and 20%. For each level of soil moisture content, the soil was molded in a Humboldt procter test cylindrical mold with the diameter of 102 mm and the height of 117 mm. The soil was compacted in three layers with a 24.5 kg rammer and 25 blows per layer. This compaction procedure stored 600 kN-m/m^3 of potential energy in the soil. Next, the soil bulk density was measured for each test, and the result was plotted versus the moisture content, as shown in Figure 3.4. A second degree polynomial line was fitted through the data points and the maximum point were determined as the maximum soil bulk density. A 100%, 85% and 70% saturation lines are also shown in Figure 3.4. The dry soil bulk density (ρ_d) corresponding to these lines are calculated using the following equation

$$\rho_d = \frac{\rho_s \rho_w}{\rho_w + w_{sat} \rho_s} \tag{3.4}$$

where ρ_s is the particle soil density equals to 2650 kg/m^3, ρ_w is the water density at 20°Celsius equals to 997 kg/m^3 and w_{sat} is the moisture content (d.b.) for 100%, 85% and 70% saturation. The maximum dry soil bulk density for the loam soil (Table 3.1) is 1670 kg/m^3 which can be obtained at 17.5% soil moisture content (d.b.).
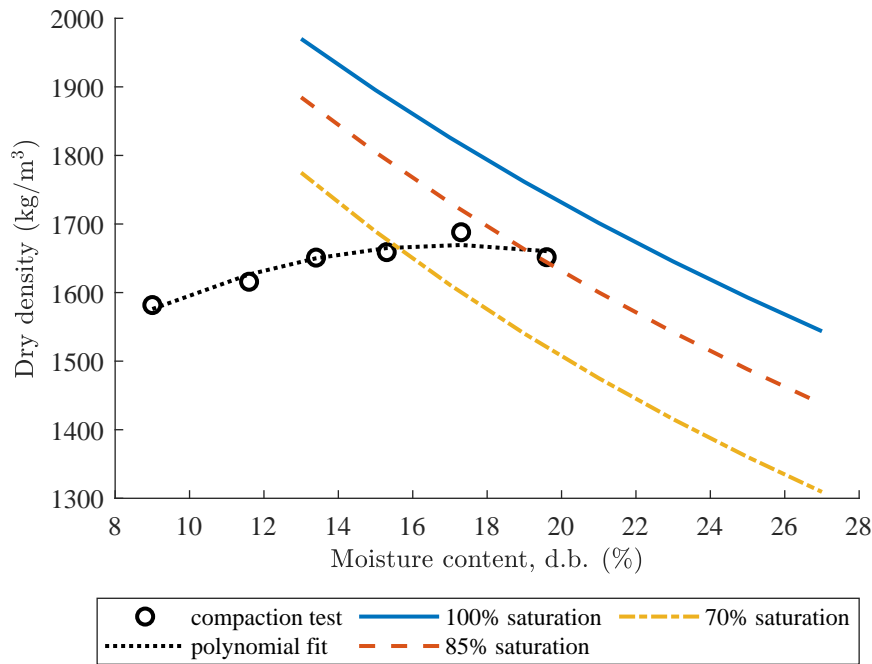
Figure 3.4: Proctor compaction test result of loam soil from Boone county, Iowa

3.1.4 Direct shear test

ASTM International (2011b) standard for a direct shear test of soils under consolidated drained condition was followed to perform the direct shear test on the loam soil. The soil was first sieved by a 4.75 mm sieve, mixed with water to reach the targeted 10% soil moisture content (d.b.), and then was poured inside a 102 mm-width square shear box and lightly compacted to reach the 1200 kg/m^3 bulk density. The direct shear test was performed at four levels of normal stresses of 61 kPa, 97 kPa, 194 kPa, and 263 kPa with three replicates for each level of normal stress. The soil specimen was sheared to 18% strain at the shearing rate of 1 mm/min. The soil moisture content (d.b. %) and soil bulk density were measured for each replicate and the average was reported as 9.97% and 1200 kg/m^3, respectively.

Figures 3.5a and 3.5b show the shear stress and the vertical deformation versus horizontal deformation. In these graphs, the average values of shear stress are shown for three replicate at

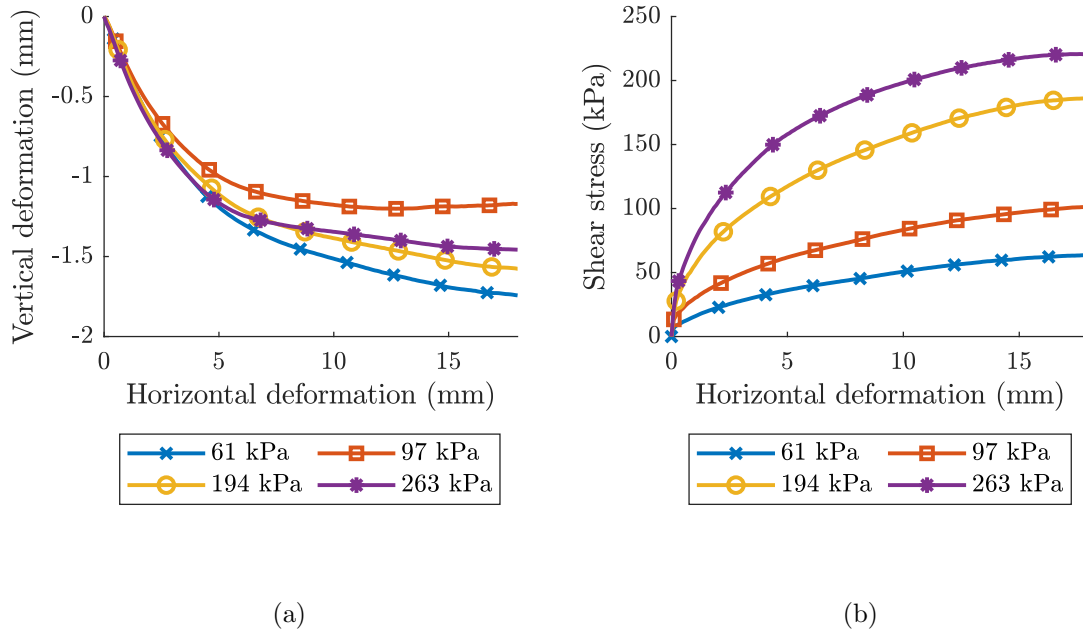(a)   (b)

Figure 3.5: a) vertical deformation and b) shear stress versus horizontal deformation at four levels of normal stresses, averaged for three replicates

each level of normal stress. To determine the soil cohesion and soil-to-soil angle of internal friction, first, the absolute maximum value of the shear stress was obtained for each replicate from the shear stress plots. Then, they were averaged for each normal stress, and a linear regression was fitted for this data. The result of this calculation is presented in Figure 3.6. The angle of the regression line based on the x-axis will give the soil-to-soil angle of internal friction, and the intercept will give the soil cohesion. The corresponding result for the direct shear test is presented in Table 3.4.

Table 3.4: Soil cohesion and soil-to-soil angle of internal friction estimated from the direct shear test for loam soil

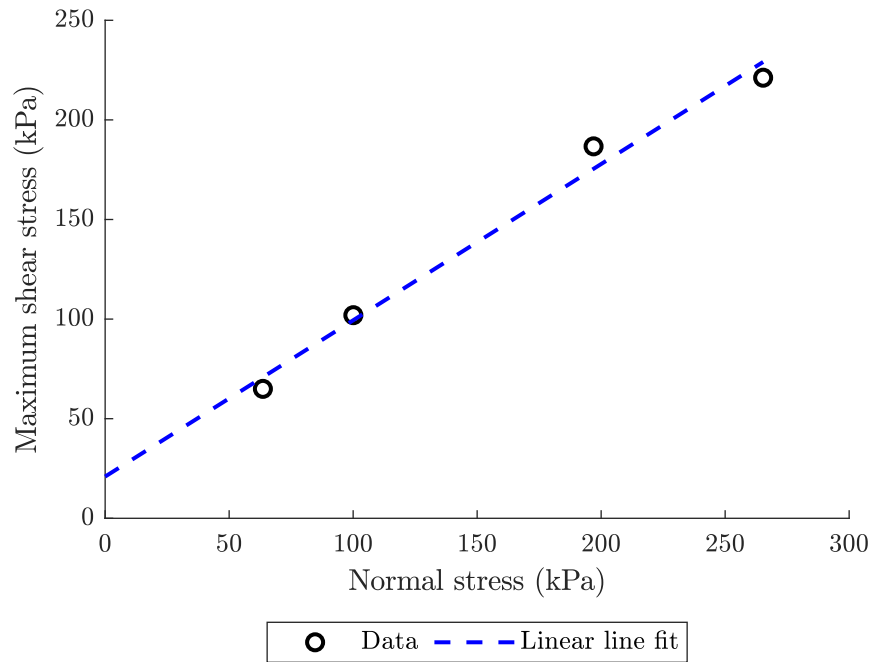| Soil cohesion (kPa)	Soil-to-soil angle of internal friction (degree)
24	38

Figure 3.6: Maximum shear stress vs. normal stress for direct shear test for loam soil

3.1.5 Triaxial test

ASTM International (2011a) standard was followed to perform a consolidated undrained triaxial compression test for loam soil. 2 mm-sieved loam soil was mixed with water to achieve desired soil moisture content. It was then molded into a cylindrical mold with 146 mm height and 72 mm diameter. The soil was poured into the mold in layers and tamped with a 24.5 kg hammer for 5 times. The procedure was continued to reach the top of the cylinder. The soil bulk density was measured. The specimen was placed in a membrane, sealed with O-rings, and placed into the triaxial test chamber. The chamber was then filled with water until no air bubbles were remained in the chamber.

Before explaining the procedure, some of the regularly used terms needs to be described.

- *Deviator stress:* The difference between the major and minor principal stresses $(\sigma_1 - \sigma_3)$

- *Back pressure:* The pressure applied to the specimen to drive the air in void space out of the specimen in order to increase the percent saturation in the specimen

- *Total pressure (σ):* The average of horizontal and vertical stress in the triaxial chamber

- *Pore pressure (u):* The pressure of the water filling the voids of the specimen

- *Effective consolidation stress (effective pressure) (σ'):* The difference between total pressure of the chamber and the pore pressure of the specimen $\sigma' = \sigma - u$

A consolidated undrained triaxial test was performed on the specimen. In this test, three phases were performed including saturation, consolidation, and shear. In the saturation phase, the void inside the specimen is filled with water without pre-stressing the specimen. In order to accomplish saturation, back pressure was applied to the specimen pore pressure to drive air out of the specimen.

In the consolidation phase, the specimen reaches the equilibrium at the desired effective stress. In order to achieve this goal, the total pressure in the chamber was increased while the back pressure was held constant until the difference between the total pressure and the back pressure was equal to the desired effective stress. The total pressure was increased by the rate of 34 kPa/min. Three different effective stresses were selected for this test which are 50 kPa, 137 kPa, and 200 kPa, and one replicate was performed for each effective stress point. The initial soil moisture content and soil bulk density were 12.57% (d.b.) and 1700 kg/m^3, respectively.

In the shear phase, the total pressure in the chamber was kept constant as the axial load piston was moved downward on top of the specimen. The pressure was applied by the strain rate of 0.075%/min until the vertical strain reached 20% of the specimen height. Since the test is undrained, the drainage from the specimen was not allowed.

Figure 3.7 shows the deviator stress versus vertical strain for the three effective stresses. The maximum value of the deviator stress, in which the failure occurs, was determined for each effective stress. The maximum deviator stress (or deviator stress at failure) was plotted with the corresponding effective stress, as shown in Figure 3.8. A linear regression was performed on the data to obtain the soil cohesion and soil-to-soil angle of internal friction. The angle of the regression line
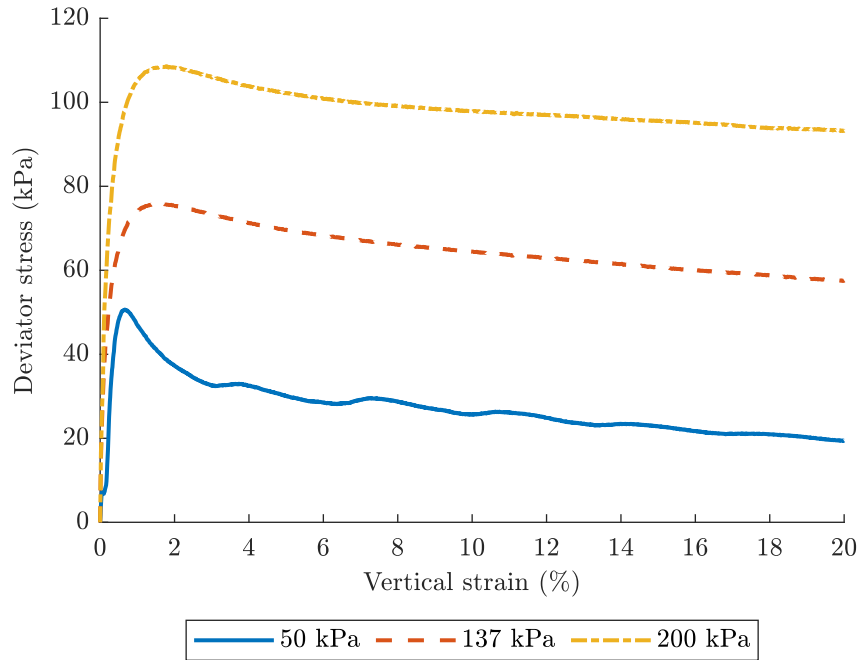
Figure 3.7: Deviator stress vs. vertical strain for triaxial test for loam soil at three levels of effective consolidation stress

to the horizontal gives the soil-to-soil angle of internal friction, and the intercept will give the soil cohesion which is presented in Table 3.5.

Table 3.5: Soil cohesion and soil-to-soil angle of internal friction estimated from the triaxial test for loam soil

Soil cohesion (kPa)	Soil-to-soil angle of internal friction (degree)
29	21

Based on Shoop (1993), the soil mechanical properties of soil cohesion and soil-to-soil angle of internal friction estimated from the triaxial test better represents the soil behavior under tire loading. Therefore, the soil cohesion and soil-to-soil angle of internal friction from the triaxial test were selected as the cohesion parameters of the loam soil.
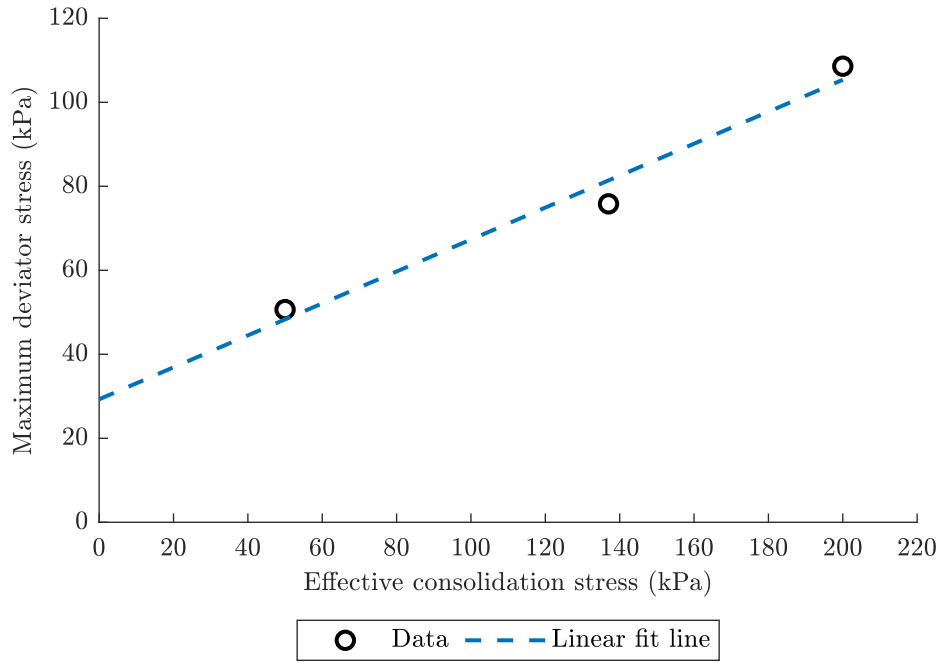
Figure 3.8: Data points of maximum deviator stress at three levels of effective consolidation stress from the triaxial test for loam soil and the linear fit line with $R^2 = 0.97$

3.1.6 Angle of repose test

Angle of repose test was performed for the loam soil using the funnel with a 32 mm orifice diameter, as shown in Figure 3.9. The funnel was loosely filled with 1.5 kg of 4.75 mm sieved loam soil with initial moisture content (d.b.) of 10.40% while the gate at the bottom of the funnel is closed. As shown in Figure 3.9, a container with 120 mm diameter and 91 mm height was centered below the funnel, where the distance between the gate and funnel orifice and the top of the container was 88 mm. Then, the gate was opened instantly and the soil flowed into the container. The procedure was repeated three times.

High resolution images were taken of all replicates from a fixed location at the end of the test when the funnel was completely emptied and the soil formed a pile in the container. These images were processed with MATLAB to determine the angle of repose. In the 2D image, the width of the
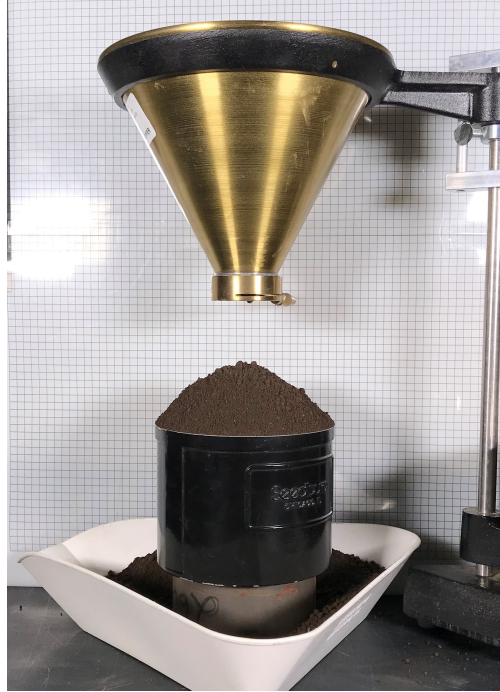
Figure 3.9: Angle of repose test with funnel orifice diameter of 32 mm and container with 120 mm diameter and 91 mm height

orifice in the funnel was subtracted from the width of the container (ASTM International, 2000). Then, two lines were drawn on the right and left side of the soil pile from the lowest point on the sides of the container to the highest point on the soil. The angle of these lines were measured, averaged between all replicates and reported as the soil angle of repose which equals to 39.3 degrees (1.7 degrees standard deviation).

3.1.7   Cone penetrometer test

ASAE Standard (1999) and ASABE Standard (1999) were followed to perform the soil cone penetrometer test on the loam soil. A FieldScout SC 900 soil compaction meter with a standard 30 degree cone with 20.27 mm diameter (ASAE Standard, 1999) was used to measure the cone penetration resistance (Figure 3.10a). A cylindrical container, 153 mm in diameter (7.5 times the ASABE cone base diameter) and 207 mm in height, was filled with 5 mm sieved moist loam soil

in three layers equal in size (Figure 3.10b). Then each layer was slightly compacted with a metal disc with the same diameter as the container to achieve the targeted soil bulk density.
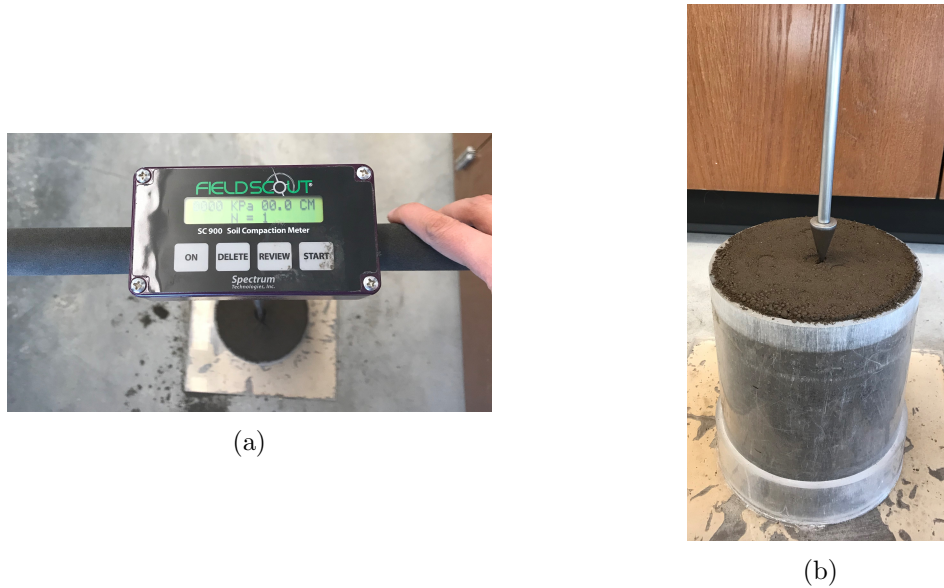

(a)

(b)

Figure 3.10: Cone penetrometer test a) device b) soil bed

The compaction meter was pushed manually into the soil at the center of the container at the rate of approximately 30 mm/s. The soil cone index (CI), which is the force per unit base area $(323\ \text{mm}^2)$ required to push the penetrometer through the soil, was acquired at every 25 mm depth increments. This procedure was repeated three times. The initial soil moisture content and soil bulk density was measured and reported as 10.41% (d.b.) and 1261 kg/m^3, respectively.

The soil cone index was plotted versus the cone depth for each replicates as shown in Figure 3.11. To measure the steady state cone index, which is where it reaches a relatively constant number, the Shape Language Modeling (SLM) (D'Errico, 2017) method was used. SLM is a curve fitting tool in MATLAB that can fit infinite number of curves to a set of data based on previous knowledge of the data using a set of shape primitives. The soil cone index versus depth graph was segmented into two sections, one a linear inclined line fit based on Equation 3.5, and the other is a constant horizontal line representing the steady state based on Equation 3.6. For each replicate, the SLM tool determined the best curve fit, the position from which the steady state started, and the steady state soil cone index. The coefficients and R-squared for three replicates are shown in
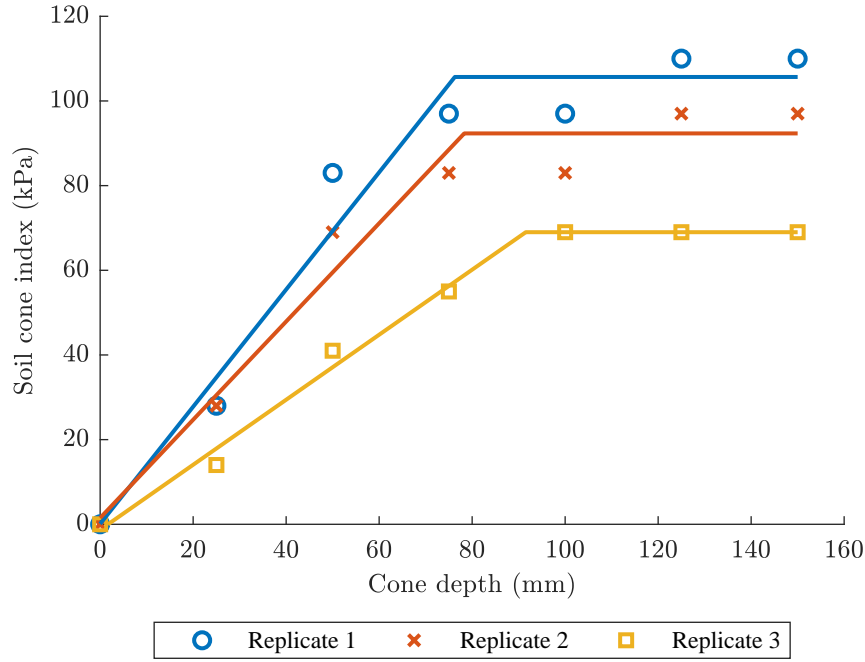
Figure 3.11: Soil cone index reading on loam soil as a function of cone depth

Table 3.6. The average of the slope of the first section was 1.1 kPa/mm (0.31 kPa/mm standard deviation) with 95% confidence interval of (0.49 , 1.72) and the steady state soil cone index was 89 kPa (18.56 kPa standard deviation) with 95% confidence interval of (52.62 , 125.38).

$$CI = a_i D + b_i \tag{3.5}$$

$$CI = c_i \tag{3.6}$$

where CI is the soil cone index, D is the cone depth, a_i and b_i are the slope and intercept of the inclined line for replicate i respectively, and c_i is a constant number which represent the steady state soil cone index for replicate i.

Table 3.6: Curve fit coefficients and R-squared for the cone penetrometer test on loam soil

Replicate	R-squared	a_i	b_i	c_i
1	0.96	1.38	0.1	106
2	0.96	1.16	1.5	92
3	0.99	0.77	-1.3	69

3.2   Soil-to-pendulum experiment

A simple test was developed for validation of the DEM soil-to-tool interaction model which includes a simple pendulum, which has a swinging motion over a soil bed. The pendulum is released from the horizontal position and cuts through the soil for a fraction of its cycle at its lowest position. The pendulum was chosen for the validation of DEM soil model because its dynamic motion is directly related to the soil reaction forces. It can also represent a single tooth in rotary tillage.

To prepare the soil for the soil-to-pendulum experiment, air-dried loam soil was sieved with 5 mm sieve and then mixed with water to reach 10% moisture content. Then a section of a soil bin with dimensions of 1016 mm length, 318 mm width and 381 mm height was loosely filled with the prepared loam soil to the height of 203 mm and 229 mm for two sets of tests with 25 mm and 50 mm cutting depth, respectively (Figure 3.12a).

As shown in Figure 3.12b the pendulum consisted of a wooden rod with 447 mm length by 90 mm width by 18 mm thickness and a steel cutting plate with 153 mm length and 101 mm width positioned at the bottom of the pendulum in a way that bottom of the plate was 25 mm lower than the bottom of the rod. Extra weights were attached at the back of the pendulum to aid penetration into the soil. The total mass of the pendulum was 13.56 kg. The pendulum was mounted to a stand with a pillow block bearing (revolute joint) to minimize the friction at the joint.

A three-axis force transducer (22 kN capacity) was placed in between the cutting plate and the rod to measure the transient soil cutting forces. An incremental encoder was attached to the pendulum at the joint to measure the angle and angular velocity. The data from both the force

transducer and the encoder was collected using a data logger (DEWE-43A, DEWSoft, Slovenia) with a sampling rate of 100 Hz.

To perform the test, the pendulum was positioned horizontally and all the sensors and encoders was balanced to zero. Then, the pendulum was released from the horizontal position and moved freely only by gravitational force. Two sets of tests with 25 mm and 50 mm cutting depth were performed. To obtained these cutting depths, the pendulum was not moved, instead, the height of the soil was changed. Five replicates were done for each set. An air-run with the pendulum in the air and without any interaction with soil was also conducted. The soil was mixed and leveled carefully to maintain the same initial soil bulk density. Soil moisture content and bulk density samples were collected after each replicate from the undisturbed section of the loam soil. The mean soil moisture content and initial soil bulk density were 9.8% and 1330 kg/m^3, respectively.
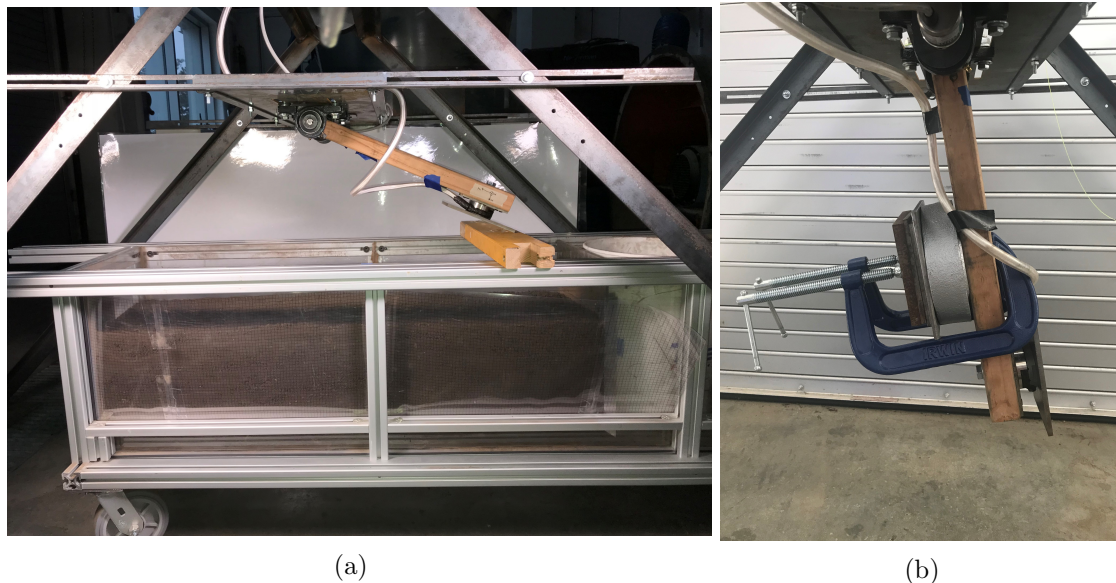

(a)   (b)

Figure 3.12: Soil-to-pendulum experiment setup a) soil bin 1016 mm length, 318 mm width and 381 mm height b) pendulum with 13.56 kg mass

3.3   Discrete Element Method (DEM) simulation

A DEM software package (EDEM Academic 2018, DEM Solution Ltd., Edinburgh, UK) was used to implement the DEM methodology for all the simulations performed in this project. For

the particle to geometry interaction, the "Hertz-Mindlin (no slip)" contact model was chosen from the built in contact models of the EDEM software. In this model, the normal force component is calculated based on Hertz (1882) contact theory, and the tangential force component is calculated based on the work of Mindlin (1949) and Mindlin and Deresiewicz (1953) (DEM Solutions Ltd, 2014) which are described is Sections 2.2.1.1 and 2.2.1.2. For the particle to particle interaction, the "Hertz-Mindlin with bonding" contact model was chosen to represent the DEM soil model. This contact model, which is based on the work of Potyondy and Cundall (2004), is explained in Section 2.2.1.5. The bond model was selected to represent the soil cohesion derived from direct shear and triaxial tests.

3.3.1 DEM soil model calibration

The cone penetrometer test and the angle of repose test were utilized to calibrate the input parameters of the DEM soil model. The cone penetrometer simulation was used to calibrate the DEM soil shear modulus and DEM soil-to-soil normal and shear stiffness which are the input parameters of the "Hertz-Mindlin with bonding" contact model. In the DEM soil model, it was assumed that the normal and shear stiffness are equal and are refer to as "bond stiffness" from this point on. After calibrating the DEM soil shear modulus and DEM soil-to-soil bond stiffness, a fraction of these calibrated values were used in the angle of repose simulation to calibrate the soil-to-soil coefficient of static friction and soil-to-soil coefficient of rolling friction.

3.3.1.1 Soil DEM model calibration using soil cone penetration resistance

For the calibration of DEM soil shear modulus and DEM soil-to-soil bond stiffness, a full factorial design of experiment (DOE) with three levels of shear modulus and four levels of bond stiffness were used to assess the statistical relationship between these DEM input parameters and the mechanical responses of virtual cone penetrometer (CP) test. The values of DEM input parameters for the cone penetrometer simulation are presented in Table 3.7. The range for soil shear modulus and bond (normal and shear) stiffness were selected based on the limits of these parameters used in

literature (Tekeste et al., 2019). To note, the Rayleigh time step (T_R) formulated as in Equation 3.7 (DEM Solutions Ltd, 2014), where R is the particle radius, ρ is the particle density, G is the soil shear modulus, and ν is the soil Poisson's ratio. Since the Rayleigh time step is related to the soil shear modulus, the percent Rayleigh time step was kept constant for all the cone penetrometer calibration simulations, although it resulted in different time steps for different shear modulus.

$$T_R = \frac{\pi R \sqrt{\frac{\rho}{G}}}{0.1631\nu + 0.8766} \tag{3.7}$$

Table 3.7: DEM input parameters for cone penetrometer simulation

DEM input parameter	Value	Unit	Source
Soil			
Poisson's ratio	0.32	-	Literature[a]
Particle density	2177	kg/m^3	Calibrated[b]
Shear modulus	1e+06, 1e+07, 1e+08	Pa	
Soil-to-soil			
Coefficient of restitution	0.01	-	Literature[a]
Coefficient of static friction	0.48	-	Literature[a]
Coefficient of rolling friction	0.4	-	Literature[a]
Soil-to-steel			
Coefficient of restitution	0.01	-	Literature[a]
Coefficient of static friction	0.31	-	Literature[a]
Coefficient of rolling friction	0.2	-	Literature[a]
HM with bonding parameter			
Normal stiffness	1e+05, 1e+06, 1e+07, 1e+08	N/m^3	
Shear stiffness	1e+05, 1e+06, 1e+07, 1e+08	N/m^3	
Bonded disk radius	2.5	mm	
Particle radius	2.5	mm	
Time step	3% Rayleigh time		

[a] Tekeste et al. (2019)
[b] Based on soil bulk density

In EDEM software, a cylinder with 153 mm diameter and 207 mm height was created and filled with 5 mm diameter single-sphere particles in three layers. The 5 mm diameter particle size was chosen for the cone penetrometer simulations to maintain the ratio of the cone diameter (B) to the DEM particles size (d_DEM) in a reasonable range (Tekeste et al., 2019). This ensured the

cone tip was always in contact with DEM particles. Each layer was slightly compacted with a disc with a velocity of 50 mm/s so that the soil reaches the same soil bulk density as the physical cone penetrometer test (1261 kg/m^3). After all layers ere compacted, the DEM soil bulk density was 1231 kg/m^3. After preparing the DEM soil bed, a cone and a rod with the same dimensions as the 30 degree ASABE standard cone (20.27 mm diameter), as in Figure 3.13, was inserted into the soil bed at the rate of 30 mm/s to the maximum depth of 150 mm from the top soil surface. The vertical forces applied on the cone were exported from the software and divided by the cone base area (323 mm^2) to obtain the soil cone index.
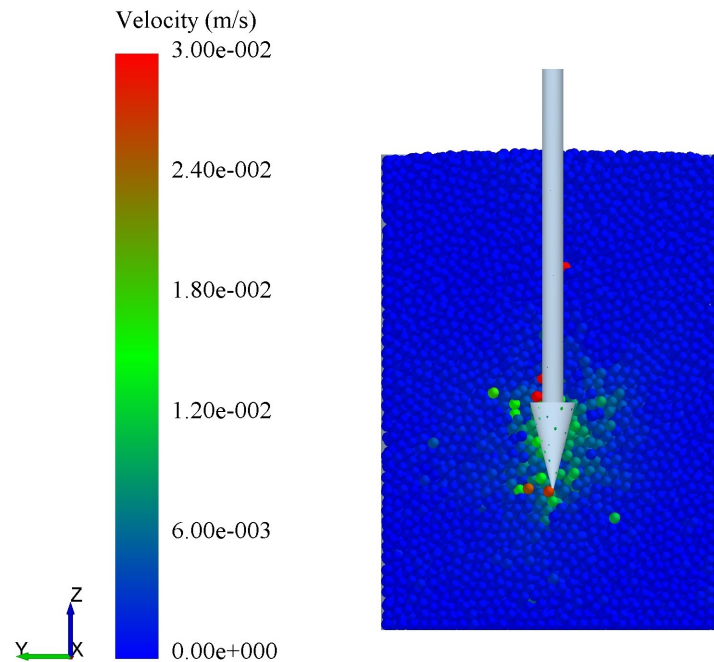

Figure 3.13: DEM simulation of ASABE standard cone penetrometer inserted in DEM soil model with 5 mm particle size, shear modulus of 1e+07 Pa and bond stiffness of 1e+05 N/m^3

To determine the steady state soil cone index for each of the simulations, the SLM code in MATLAB was used which is explained in section 3.1.7. Using the depth intervals obtained from the physical cone penetrometer test, the inclined line and steady state (horizontal) sections of each

simulation were determined. The slopes of the inclined line and the values of the steady state were recorded for comparison with physical test. MATLAB was also used to assess the marginal effects of the DEM soil shear modulus and the soil-to-soil bond stiffness on the steady state soil cone index.

A statistical analysis software (JMP Pro 14.1, SAS Institute Inc., Cary, NC) was used to perform more statistical analysis and optimization procedure. The standard least squares approach was selected to fit a multiple regression model into the cone penetrometer data. In this approach, the sum of squared residuals, which is the difference between an observed value and the fitted value provided by a model, is minimized. The profiler tool in JMP Pro 14.1 was also used to find the optimum values of DEM soil shear modulus and soil-to-soil bond stiffness to obtain the closest DEM soil cone index to the experimental one. In the profiler, first, a desirability function is formed based on three defining point (low, middle and high) which are called control points (SAS Institute Inc, 2018). The average steady state soil cone index and 95% confidence interval from the experimental test were set as the control points in the profiler. Based on SAS Institute Inc (2018) documentation, JMP profiler uses the gradient descent algorithm to optimize the overall desirability function for continuous variable (which is the current case).

3.3.1.2   Soil DEM model calibration using angle of repose

For the calibration of soil-to-soil coefficient of static friction and rolling friction, a full factorial design of experiment with three levels of each parameters were used to find the optimum values which best represent the angle of repose of the loam soil. The values of DEM input parameters for the angle of repose (AOR) simulation are presented in Table 3.8. The range for coefficient of static friction was selected based on literature and laboratory tests. 0.45 was selected as middle point based on Tekeste et al. (2019), and the lower and upper limits were selected based on the soil-to-soil angle of internal friction (ϕ) determined from direct shear test and triaxial test (coefficient of static friction = $\tan(\phi)$). The range of coefficient of rolling friction was selected based on the lower and upper limit of this value used in literature (Tekeste et al., 2019).

Table 3.8: DEM input parameters for angle of repose simulation

DEM input parameter	Value	Unit	Source
Soil			
Poisson's ratio	0.32	-	Literature[a]
Particle density	2177	kg/m^3	Calibrated[b]
Shear modulus	4.71e+07	Pa	Calibrated[c]
Soil-to-soil			
Coefficient of restitution	0.01	-	Literature[a]
Coefficient of static friction	0.25, 0.45, 0.65	-	
Coefficient of rolling friction	0.01, 0.40, 1.00	-	
Soil-to-steel			
Coefficient of restitution	0.01	-	Literature[a]
Coefficient of static friction	0.31	-	Literature[a]
Coefficient of rolling friction	0.2	-	Literature[a]
HM with bonding parameter			
Normal stiffness	1e+05	N/m^3	Calibrated[c]
Shear stiffness	1e+05	N/m^3	Calibrated[c]
Bonded disk radius	2.5	mm	
Particle radius	2.5	mm	
Time step	3% Rayleigh time		

[a] Tekeste et al. (2019)

[b] Based on soil bulk density

[c] Based on cone penetration resistance

A CAD (2016, Solidworks, Waltham, MA) drawing of the angle of repose apparatus was created with the same dimensions as the physical device except for the funnel orifice which was scaled with the scale factor of 1.5. This scaling was done based on primary exploratory simulations with 5 mm diameter single-sphere DEM soil particles with the original and scaled orifice diameter to investigate the flowability of the DEM soil through the orifice. The 5 mm diameter particle size was chosen to be consistent with the Cone penetrometer simulations. In EDEM software, using a Hertz-Mindlin with bonding contact model, the funnel was filled with 1.5 kg. After the soil particles reached equilibrium, the orifice was opened and the particles flowed into a container underneath the orifice with 120 mm diameter and 91 mm height. The distance between the container and the orifice was set to 80 mm. The simulation was continued until all particles were discharged from the funnel,

formed a pile in the container and reached a stable state where no particles rolling down the pile, as shown in Figure 3.14.
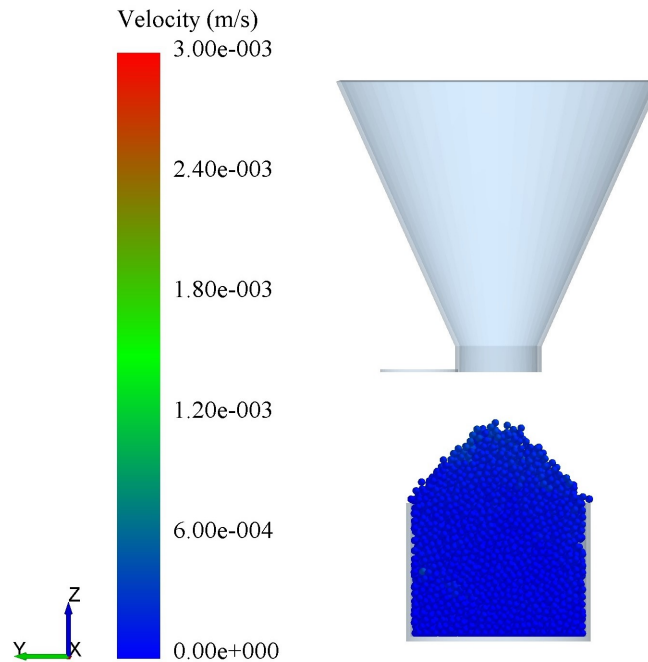

Figure 3.14: EDEM simulation of angle of repose from a DEM soil model with 5 mm particle size, coefficient of static friction of 0.45 and coefficient of rolling friction of 0.4

To measure the angle of repose, a rectangular grid, with the same length as the container diameter and width of 10 mm, was created in the middle of the container. The grid was sectioned into twenty six 5 mm grids so that each section had a same width as the DEM soil particle diameter. The height of the maximum particle inside each of these 5 mm grids were exported from the software and used as data points to measure the angle. The same procedure as in the physical angle of repose test (Section 3.1.6) was followed to measure the angle of repose for all the DEM simulations.

A programming language (MATLAB 2017, MathWorks Inc, Natick, MA) was used to perform the line fitting and measuring the angle of repose. This software was also used to assess the marginal effect of the soil-to-soil coefficient of static friction and rolling friction on the virtual angle of repose.

The JMP Pro 14.1 software was used to perform additional statistical analysis and optimization procedure. As explained in the previous section the standard least square approach was used for the multiple regression model, and the average angle of repose and the 95% confidence interval from the physical test were used as control points for profiler tool.

3.3.2 DEM simulation of soil-to-pendulum interaction

Soil-to-pendulum interaction was simulated using a DEM model. A soil box with 1016 mm length, 318 mm width and 381 mm height (same as the physical experiment of the soil-to-pendulum system) was modeled in EDEM software. It was filled with DEM soil particles in two layers. The bottom layer of DEM soil was 127 mm in height and consisted of 10 mm single-sphere particles. The top layer was 76 mm and 102 mm in height which resulted in 203 mm and 229 mm total soil depth for 25 mm and 50 mm cutting depth, respectively. The top layer was comprised of four different particle sizes based on a distribution derived from the physical particle size distribution of the loam soil (Figure 3.3). Using the loam soil particle size distribution, the d_{50} (which is the diameter of the soil particles that 50% of soil sample's mass is smaller than) was found and scaled by 6.4 to obtain 5 mm DEM particle size. This scaling was done to represent the median size of the loam soil with 5 mm DEM particle size (which was used in cone penetrometer and angle of repose calibration simulations). Then, d_{40}, d_{60} and d_{70} were also determined and scaled by 6.4 to obtain a distribution for DEM soil particles (Table 3.9). Each layer of soil was slightly compacted with a flat plate to level the soil surface and achieve the same bulk density as in physical test (1330 kg/m^3). The initial DEM soil bulk densities of the top layer were 1373 kg/m^3 and 1378 kg/m^3 for 76 mm and 102 mm height, respectively.

The CAD geometry of the pendulum (Figure 3.15b) with the rod dimensions of 447 mm by 90 mm by 18 mm and the cutting plate with dimensions of 153 mm height and 101 mm width, was imported to EDEM. The pendulum was positioned horizontally (Figure 3.15a) in a way that, when reaching the minimum position, it would cut the soil at 25 mm and 50 mm cutting depth for soil depth of 203 mm and 229 mm, respectively. The pendulum center of mass was determined

Table 3.9: DEM soil particles sizes

D-value	Physical size (mm)	DEM size (mm)	Percent mass (%)
Top layer (distribution) - 76 mm and 102 mm (for 25 and 50 mm cutting depth) height			
d_{40}	0.53	3.4	25
d_{50}	0.78	5.0	25
d_{60}	1.15	7.37	25
d_{70}	1.68	10.77	25
Bottom layer - 127 mm height			
		10	100

using the pendulum geometry and all the extra weights (Figure 3.12b), and implemented in EDEM software; however, the visual representation of the weights was not included in the CAD geometry EDEM.
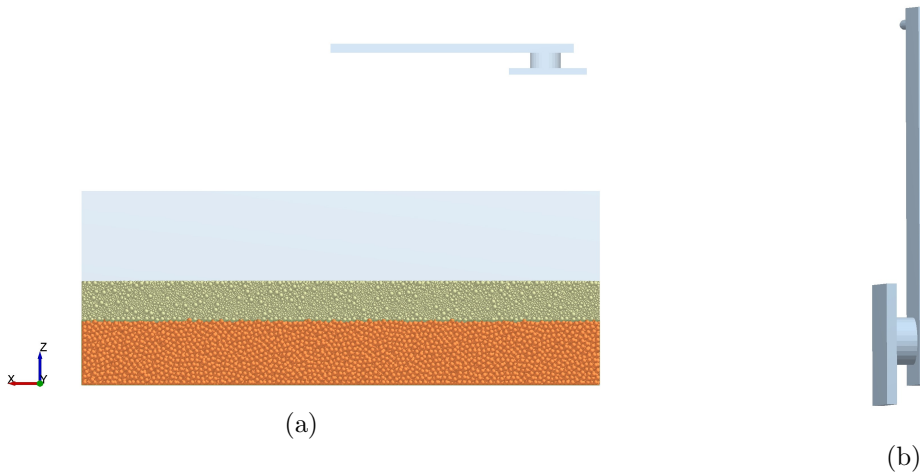

(a)

(b)

Figure 3.15: a) DEM soil-to-pendulum simulation b) Pendulum geometry

For the dynamic motion of the pendulum, the sinusoidal rotation was chosen from the embedded kinematics of the EDEM software. This sinusoidal rotation were derived from the physical experiment of the pendulum motion in the air-run (without interaction with soil) in a way that the frequency and the amplitude of the position of the pendulum in EDEM matched the one in the experiment. The sinusoidal equation of the pendulum motion in EDEM is as follow

$$\theta = A \, sin(2\pi ft - \phi) + A \qquad (3.8)$$

where θ is the angle of the pendulum in degree at time t, A is the amplitude which equals π, f is the frequency which equals 0.75, and ϕ is the phase which equals $\pi/2$.

The DEM input parameters to simulate the soil-to-pendulum test is presented in Table 3.10. The time step was chosen as 3% Rayleigh time which equals 1.173e-06 seconds and the simulation was run for half a cycle of pendulum rotation which is equivalent to 0.66 seconds.

Table 3.10: DEM input parameters for soil-to-pendulum simulation

DEM input parameter	Value	Unit	Source
Soil			
Poisson's ratio	0.32	-	Literature[a]
Particle density	2177	kg/m^3	Calibrated[b]
Shear modulus	4.71e+07	Pa	Calibrated[c]
Steel			
Poisson's ratio	0.3	-	EDEM default[d]
Particle density	7800	kg/m^3	EDEM default[d]
Shear modulus	7e+10	Pa	EDEM default[d]
Soil to soil			
Coefficient of restitution	0.01	-	Literature[a]
Coefficient of static friction	0.45	-	Calibrated[e]
Coefficient of rolling friction	0.4	-	Calibrated[e]
Soil to steel			
Coefficient of restitution	0.01	-	Literature[a]
Coefficient of static friction	0.31	-	Literature[a]
Coefficient of rolling friction	0.2	-	Literature[a]
HM with bonding parameter			
Normal stiffness	1e+05	N/m^3	Calibrated[c]
Shear stiffness	1e+05	N/m^3	Calibrated[c]
Bonded disk radius	2.5, 5	mm	
Particle radius	various	mm	
Time step	3% Rayleigh time		

[a] Tekeste et al. (2019)

[b] Based on soil bulk density

[c] Based on cone penetration resistance

[d] Based EDEM material database for steel

[e] Based on angle of repose

3.3.3 DEM-MBD co-simulation of soil-to-pendulum interaction

Since DEM simulations can not account for the reaction forces from the DEM soil particles, Multibody Dynamics (MBD) method was coupled with DEM. For this co-simulation, DEM software package (EDEM Academic 2018, DEM solutions Ltd., Edinburg, UK) was used to simulate the soil particles, and a multibody modeling software (LMS Virtual.Lab Motion 13.8, Siemens Inc., Plano, TX) was used to model the dynamics of the pendulum. In the coupling simulation, velocity and position of the pendulum are calculated in LMS Virtual.Lab Motion and then transferred to EDEM in which reaction forces from soil particles are updated and sent back to LMS Virtual.Lab Motion.
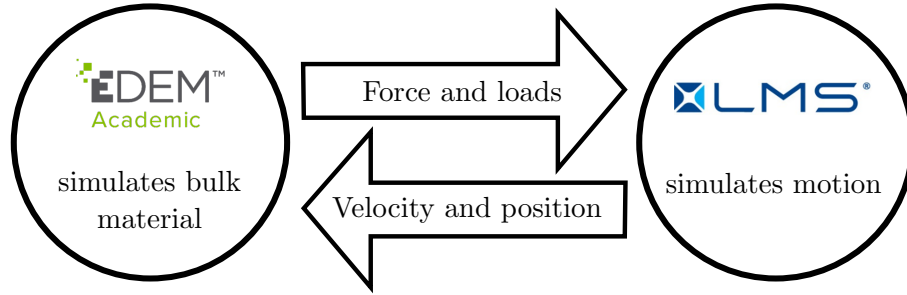

Figure 3.16: Workflow diagram of EDEM-LMS Virtual.Lam Motion coupling

The soil-to-pendulum system was simulated using the DEM-MBD coupling. The DEM soil particle size (shown in Table 3.9) and soil properties (shown in Table 3.10) are similar to the DEM-only model. The DEM particle generation and preparation were also the same as described in 3.3.2, with 10 mm DEM soil particles in the bottom layer and a scaled size distribution for the top layer. There was no need to model the soil particles in the LMS Virtual.Lab Motion.

As shown in Figure 3.17a, in LMS Virtual.Lab Motion, the top plate of the stand was created as a fixed body and the pendulum geometry was created with the same dimensions and mass to the experiment setup. The pendulum was connected to the fixed body with a revolute joint which has a rotational damper actuator with only a rotational damping coefficient of 1 $\frac{kg.m^2}{s.rad}$. The damping coefficient was calibrated based on the pendulum motion in air (without interaction with soil) in soil-to-pendulum experiment. The mass, moment of inertia and center of mass of the pendulum were specified in the LMS.Virtual Lab Motion and the pendulum was positioned horizontally at the
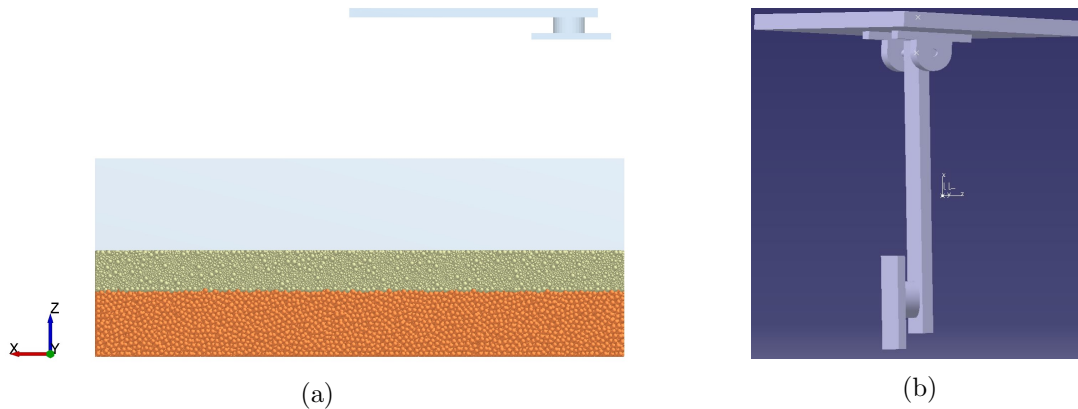
Figure 3.17: a) DEM-MBD soil-to-pendulum co-simulation in EDEM b) Pendulum geometry in LMS Virtual.Lab Motion

beginning of the simulation. The same pendulum geometry without the fixed stand was imported in EDEM software in a way that its initial position and the center of mass matched the pendulum in LMS Virtual.Lab motion.

The pendulum motion was solely based on the gravitational force. When the pendulum contact the soil particles, the soil reaction forces act as external forces applied on the cutting plate and affect the motion of the pendulum. The simulation was run for 0.7 seconds which is half a cycle of pendulum rotation. The time step in EDEM was chosen as 3% Rayleigh time which equals 1.173e-06 seconds and the LMS Virtual.Lab Motion time step was matched to the same number. The simulation was run for 25 mm and 50 mm cutting depths.

CHAPTER 4.   RESULTS AND DISCUSSION

4.1   Soil-to-pendulum experiment

The pendulum motion was analyzed for all the replicates at the first half cycle. Figure 4.1 shows the position and angular velocity of the pendulum at two cutting depths of 25 mm and 50 mm. The pendulum motion is affected by the soil reaction forces and this effect is more extreme at the 50 mm cutting depth. As shown in Figure 4.1b, the pendulum angular velocity has a larger change at the 50 mm cutting depth comparing to the 25 mm one.

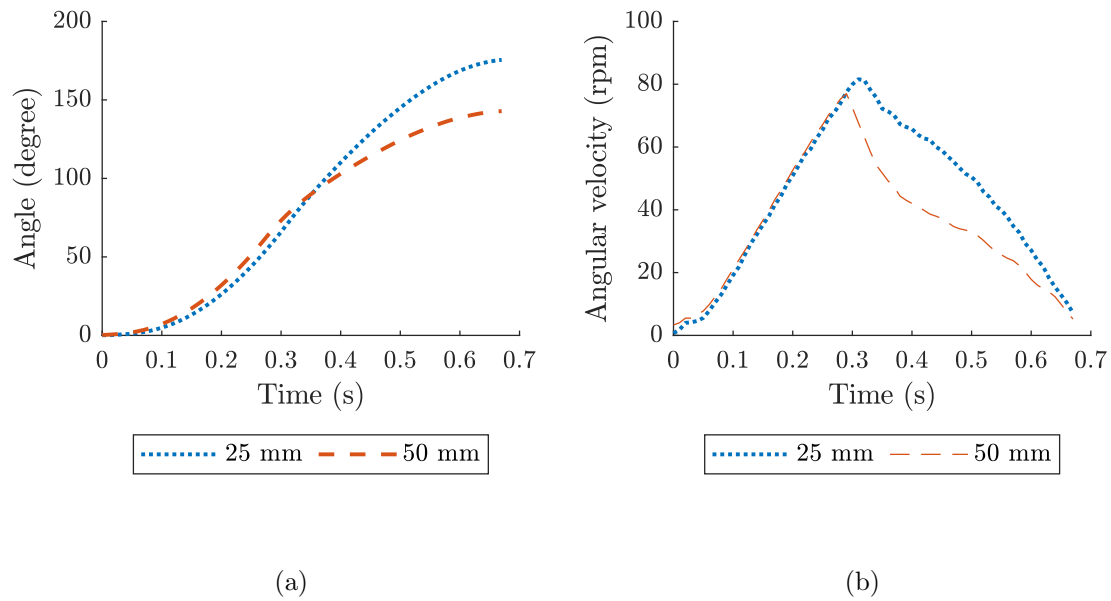(a)   (b)

Figure 4.1: Pendulum a) angle b) and angular velocity from soil-to-pendulum experiment at two cutting depths

In the soil-to-pendulum experiment, the force transducer measures normal and tangential forces applied on the cutting plate. The free body diagram (Figure 4.2) of the pendulum at angle θ was used to convert the normal and tangential forces measured by the transducer to the horizontal (F_h)

and vertical (F_v) forces for all data points, using following equations

$$F_h = F_y \ cos\theta + F_z \ sin\theta \tag{4.1}$$

$$F_v = F_y \ sin\theta - F_z \ cos\theta \tag{4.2}$$

where F_y and F_z are the tangential (parallel to the pendulum) and normal (normal to the pendulum) forces on the cutting plate, respectively.
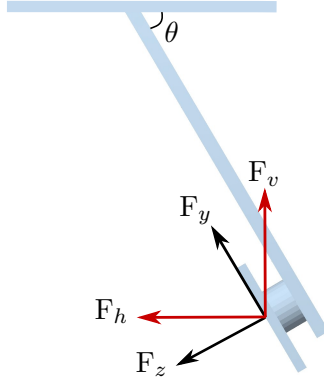

Figure 4.2: Free body diagram of the pendulum

The maximum horizontal and vertical forces occur at the first impact of the pendulum to the soil within the first half cycle. To obtain the soil cutting forces, the effect of pendulum mass, which was captured in the pendulum test in the air, was subtracted from the measured forces. As shown in Figure 4.3, the maximum horizontal force on the cutting plate in the soil-to-pendulum replicates was determined (point 1). Then the corresponding horizontal force at the same angle in the air replicate was detected (point 2). The difference between these two values gives the maximum horizontal soil cutting force. Similarly, the vertical soil cutting force was obtained by determining the maximum vertical force from soil-run and the vertical force at the same angle from air-run and subtracting them. This procedure was repeated for all replicates for both cutting depths. The results of the maximum soil cutting forces are shown in Table 4.1.

In Table 4.1, the negative sign for the horizontal forces and the positive sign for the vertical forces represent a compressive force normal to the cutting plate and an upward force parallel to the cutting plate along the linkage arm, respectively. The maximum horizontal and vertical soil
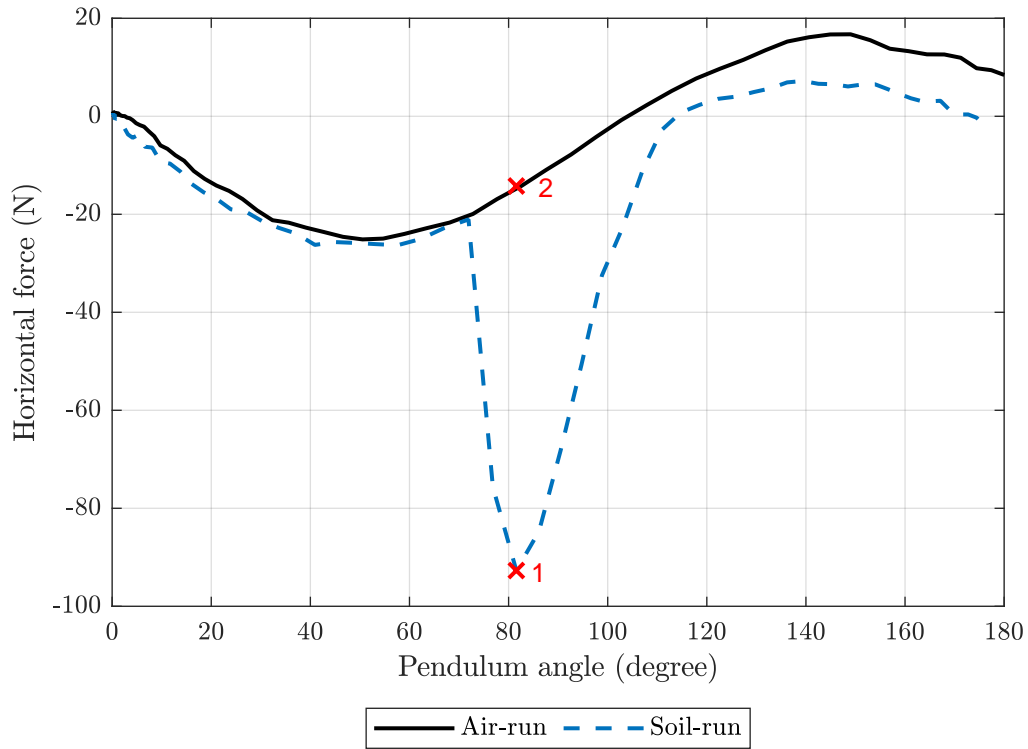
Figure 4.3: The horizontal forces on the cutting plate in soil-to-pendulum experiment in air-run and soil-run at 25 mm cutting depth

cutting forces are higher from the 50 mm cutting depth comparing to the forces from the 25 mm cutting depth. This increase in forces by depth might be associated with the increased contact area and soil surcharge in front of the pendulum. The 50 mm cutting depth test has 13 degrees lower angle at the maximum cutting forces than the 25 mm cutting depth test. Table 4.2 shows the soil horizontal and vertical forces at 90 degrees, where the pendulum is at the maximum cutting depth and the maximum contact area at the soil and blade interface.

Table 4.1: Maximum soil horizontal and vertical forces and corresponding angle from soil-to-pendulum experiment

Cutting depth (mm)	Horizontal force (N)		Vertical force (N)		Angle (degree)	
	Mean	SD	Mean	SD	Mean	SD
25	-73	9	38	7	83	1
50	-108	9	85	12	70	2

Table 4.2: Soil horizontal and vertical forces at 90 degrees from soil-to-pendulum experiment

Cutting depth (mm)	Horizontal force (N)		Vertical force (N)	
	Mean	SD	Mean	SD
25	-60	12	28	6
50	-62	10	38	7

4.2   DEM soil model calibration

4.2.1   Soil DEM model calibration using cone penetration resistance

The marginal effect of the shear modulus and the bond stiffness were studied on the steady state soil cone indexes for all DOE points. The result are shown in Figure 4.4 and 4.5 where the x-axes are in logarithmic scale to give a better representation of the data points. As shown in Figure 4.4, the shear modulus has a logarithmic relationship with the steady state soil cone index, where, as shown in Figure 4.5, the bond stiffness has a linear relationship with the steady state soil cone index. Therefore, the logarithm of the shear modulus to base 10 ($log_{10}(G)$) was used for all further statistical analysis.

In the JMP Pro 14.1 software, a multiple regression model was created with the bond stiffness (k) and the logarithm of shear modulus ($log_{10}(G)$) as the two explanatory variables with the interaction effect, and with the steady state soil cone index (CI) as the response variable. This model fits the data with the R-squared of 0.99, and the parameters estimation are presented in Table 4.3.

In this model, the intercept estimate shows the value of the soil cone index when all other explanatory variables are zero. However, the intercept and the bond stiffness estimations are not
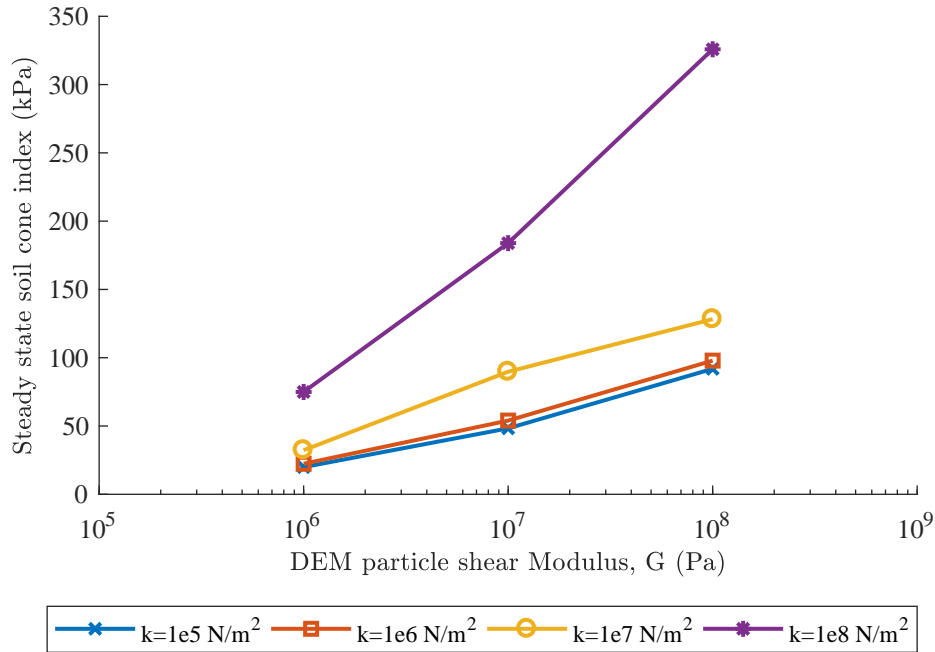
Figure 4.4: Marginal effect of shear modulus on steady state cone index for four levels of normal stiffness

interpretable here because the soil shear modulus cannot be zero in the DEM model. The shear modulus estimate shows that the expected increase in the soil cone index is 37.24 kPa for each ten-fold increase in the shear modulus.

The profiler tool in the JMP software was used to find the optimum values of the shear modulus and the bond stiffness based on the multiple regression model. In this tool, the average steady state soil cone index (89 kPa) and the 95% confidence interval (52.62,125.38) derived from the physical test (Section 3.1.7) were set as the control points (the target, the minimum, and the maximum values). As a result, the optimum values derived from the cone penetrometer calibration for the shear modulus and the bond stiffness are 4.71e+06 Pa and 3.87e+07 N/m^3 respectively.

To verify these optimum values, another DEM cone penetrometer simulation was run with the new values for shear modulus and the bond stiffness where all other input parameters remained
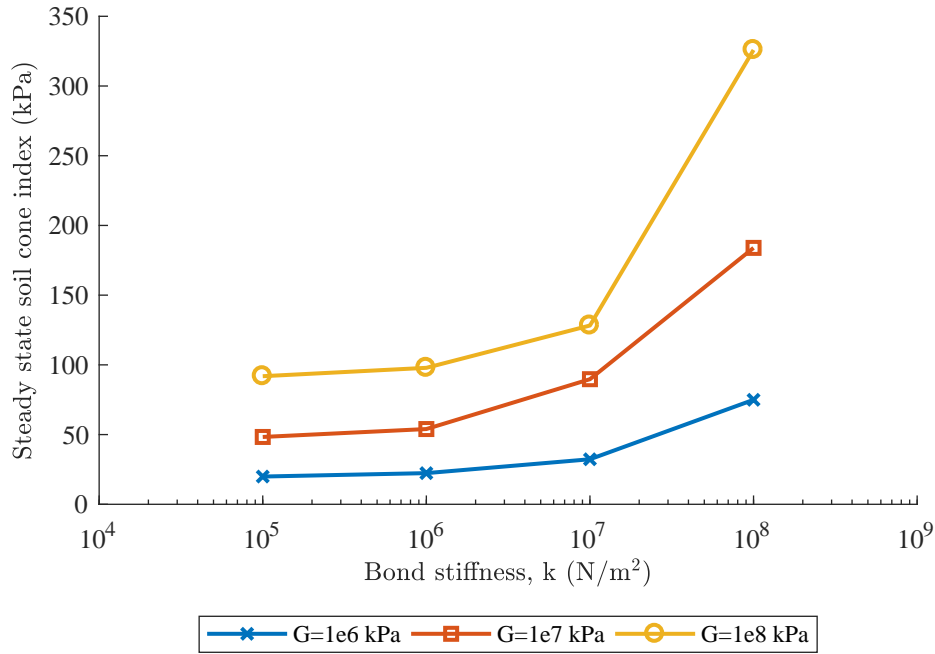
Figure 4.5: Marginal effect of normal stiffness on steady state cone index for three levels of shear modulus

constant. The same procedure as explained in Section 3.3.1.1 was followed for the data extraction and analysis for the DEM simulation. The slope of the first section was 1.3 and the steady state soil cone index was 99 kPa, which had 19% and 12% error, respectively, compared to the physical test with the slope of 1.1 and the steady state soil cone index of 89 kPa.

The optimum bond stiffness derived from the cone penetrometer calibration was so high for the DEM soil particles to flow through the hopper orifice in the angle of repose simulation. Therefore, further cone penetrometer DEM simulations were run with a fraction of the optimum bond stiffness to find new optimum values. To compensate for the decrease in the normal stiffness, the shear modulus was increased to find the best combination of these two DEM input variables to obtain the closest steady state soil cone index to the physical test. The final optimum values found with this procedure are 4.71e+07 Pa for the shear modulus and 1e+05 N/m^3 for bond stiffness with -2%

Table 4.3: Parameter estimates for the multiple regression model of the cone penetrometer calibration data

Term	Estimate	Standard error	t ratio	probability$> |t|$
Intercept	-201.09	29.47	-6.82	0.0001
k	-4.83e-6	5.87e-7	-8.23	<0.0001
$log_{10}(G)$	37.24	4.18	8.90	<0.0001
k*($log_{10}(G)$)	8.84e-7	8.32e-8	10.62	<0.0001

error in the slope and -11% error in the steady state soil cone index. These values were used in the angle of repose calibration DOE and represented in Table 3.8.

4.2.2 Soil DEM model calibration using angle of repose

The marginal effect of the coefficient of static friction and the coefficient of rolling friction were studied on the soil angle of repose for all DOE points. The results are shown in Figure 4.6 and 4.7. In the JMP Pro 14.1 software, a multiple regression model was created with the coefficient of static friction (SF) and the coefficient of rolling friction (RF) as the two explanatory variables with the interaction effect, and with the soil angle of repose (AOR) as the response variable. This model fits the data with the R-squared of 0.76, and the parameters estimation are presented in Table 4.4.

Table 4.4: Parameter estimates for the multiple regression model of the angle of repose calibration data

Term	Estimate	Standard error	t ratio	probability$> |t|$
Intercept	10.07	8.76	1.15	0.3026
SF	31.20	17.03	1.83	0.1264
RF	22.73	6.83	3.23	0.0208
SF*RF	49.99	41.83	1.20	0.2856

In this model, the intercept estimate shows the value of the soil angle of repose when all other explanatory variables are zero, meaning when the coefficients of static and rolling friction are zero, the predicted angle of repose is 10.07 degrees based on this regression model. Also, increasing the
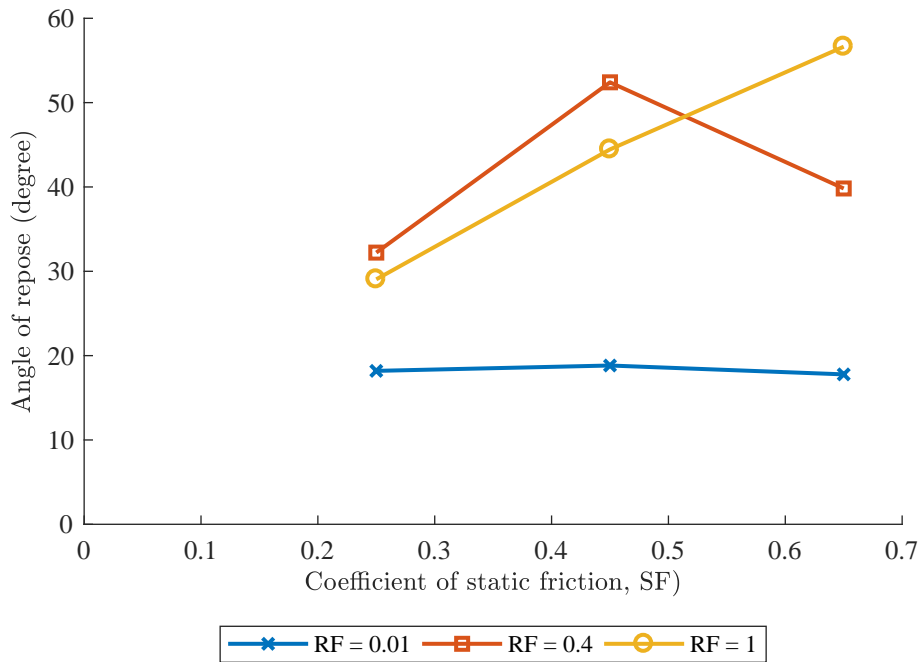
Figure 4.6: Marginal effect of coefficient of static friction on soil angle of repose for three levels of coefficient of rolling friction

coefficients of static friction and rolling friction by 1 results in an expected increase of the angle of repose by 31.20 and 22.73 degrees, respectively.

The profiler tool in the JMP software was used to find the optimum values of the coefficients of static and rolling friction according to the multiple regression model. In this tool, the average angle of repose (39 degrees) and the 95% confidence interval (36,43) obtained from the physical test (Section 3.1.6) were set as control points (the target, the minimum, and the maximum values). As a result, the optimum values derived from the angle of repose calibration for the coefficient of static friction and the coefficient of rolling friction are 0.45 and 0.68, respectively.

To verify these optimum values, another DEM simulation for the angle of repose was run with optimal values for coefficients of static friction and rolling friction and all other DEM input parameters remained the same. The similar procedure as explained in Section 3.3.1.2 was followed
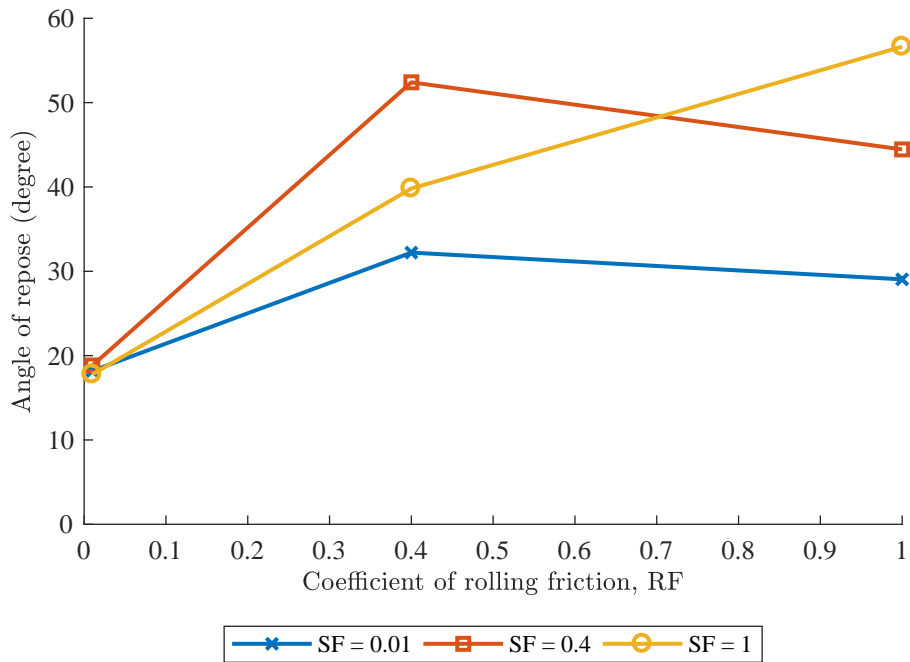
Figure 4.7: Marginal effect of coefficient of rolling friction on soil angle of repose for three levels of coefficient of static friction

for the data extraction and analysis for the DEM simulation. The DEM angle of repose is 49 degrees which had 24% error compared to the physical test. Since this amount of error was too high, a few additional DEM angle of repose simulations were run to achieve a lower DEM angle of repose. These simulations had lower values of coefficient of rolling friction and all other DEM input parameters remained the same. The coefficient of rolling friction was lowered until the best combination of coefficients of static friction and rolling friction was achieved that gave the closest soil angle of repose to the physical test. These values are 0.45 and 0.3 for coefficients of static and rolling friction, respectively.

4.2.3 DEM calibrated soil model

As the final verification of the optimum values obtained from the cone penetrometer and angle of repose calibration, the DEM cone penetrometer simulation was run with the calibrated values shown in Table 4.5. The rest of the parameters remained the same as in Table 3.7. The same procedure as explained in Section 3.1.7 and Section 3.3.1.1 were followed to obtain the results. The slope of the first section is 1.05 and the steady state soil cone index is 77 kPa which have -4% and -14% error, respectively, comparing to the physical test. Therefore, these optimum values were chosen as the calibrated input parameter for DEM soil model and used in further DEM validation simulations.

Table 4.5: DEM calibrated input parameters

DEM input parameter	Value	Unit
Shear modulus (G)	4.71e+07	Pa
Coefficient of static friction (SF)	0.45	-
Coefficient of rolling friction (RF)	0.3	-
Normal stiffness (k)	1e+05	N/m^3
Shear stiffness (k)	1e+05	N/m^3

4.3 DEM simulation of soil-to-pendulum interaction

The position and the angular velocity of the pendulum were analyzed for the DEM simulation of soil-to-pendulum interaction. As shown in Figure 4.8, the position and the angular velocity of the pendulum are exactly matched at 25 mm and 50 mm cutting depths. They are also similar to the input sinusoidal equation (Equation 3.8) for the pendulum motion, and the soil reaction forces do not have any effect on the position and velocity of the pendulum in DEM simulations.

In DEM simulations, the horizontal and vertical forces from the soil particles on the cutting plate were directly exported from EDEM software. As shown in Figure 4.9a, the horizontal soil cutting forces have negative values which represent the compressive force toward the cutting plate. The horizontal force for 50 mm cutting depth is higher than the one for 25 mm cutting depth which

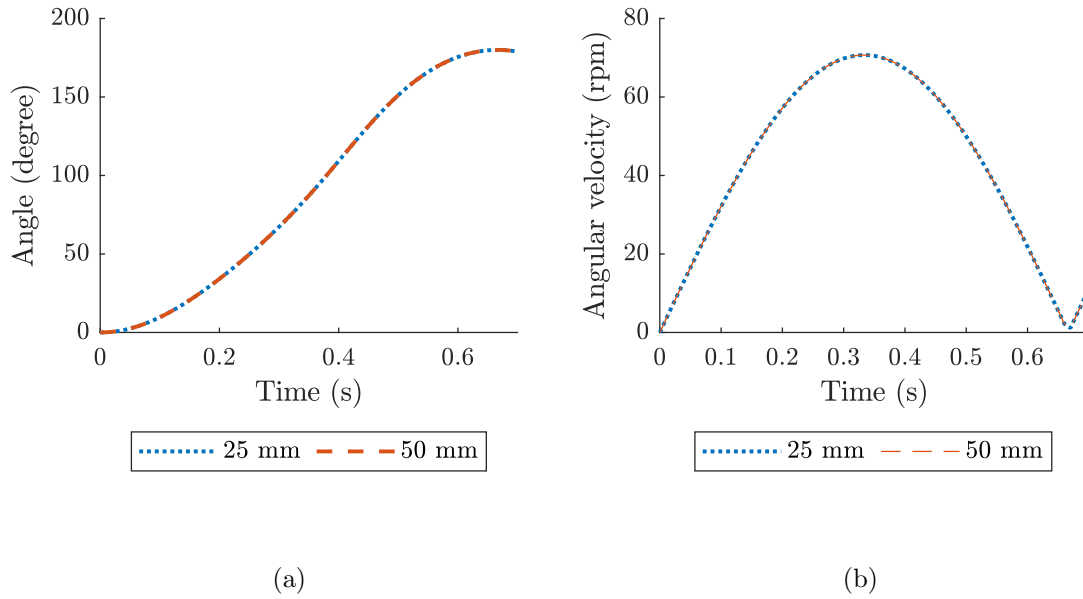(a)   (b)

Figure 4.8: Pendulum a) angle b) and angular velocity from the DEM simulations of soil-to-pendulum interaction at two cutting depths

matches the same trend for the experiment. As presented in Figure 4.9b, the vertical soil cutting forces are positive which show upward force from the soil. The vertical force for 50 mm cutting depth is also higher than for 25 mm which also matches the trend for the experiment. Also, the entry angles for 25 mm and 50 mm cutting depths are 60 degrees and 53 degrees, respectively.

The maximum values for horizontal and vertical forces were determined, and are shown in Table 4.6. Also, the horizontal and vertical forces at 90 degrees from the initial horizontal position are presented in Table 4.7. Similar to the soil-to-pendulum experiment (Table 4.1), the direction of the maximum soil cutting forces are compressive for horizontal forces, and upward from the soil for vertical forces. The magnitude of both the DEM predicted horizontal and vertical forces are remarkably higher comparing to the experiment. This overprediction might be due to the active pendulum motion through the DEM soil particles. In the experiment, the pendulum motion and velocity are dominated by the amount of soil reaction forces applied to the pendulum. These forces reduce the velocity of the pendulum which results in lower soil reaction forces from soil further in the movement of the pendulum. While in the simulation, the input motion of the pendulum was

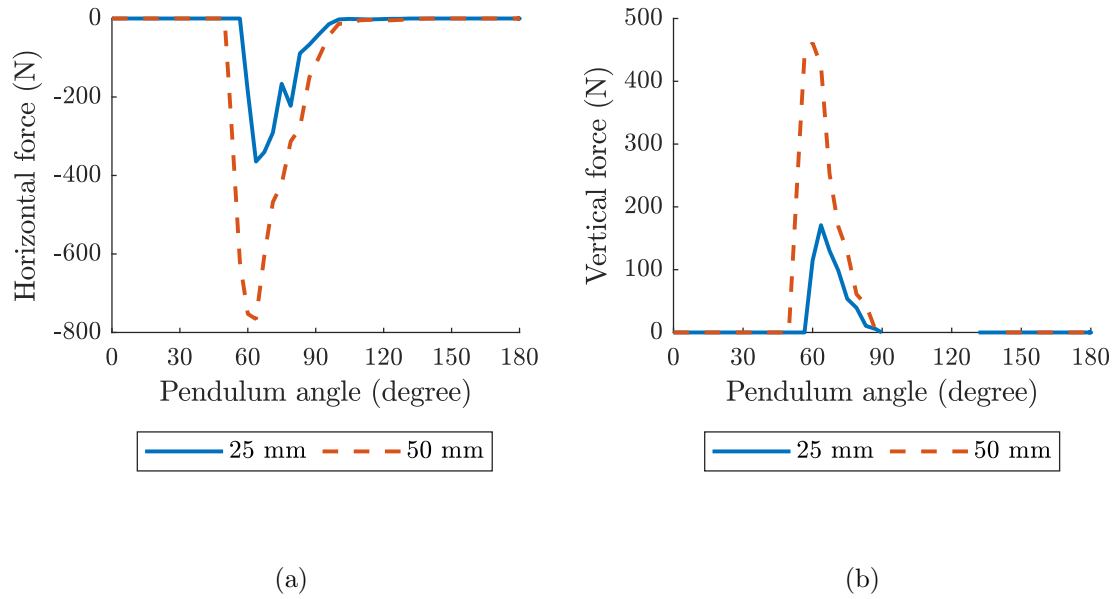(a)   (b)

Figure 4.9: Comparison of a) horizontal and b) vertical soil cutting force from the DEM simulation of soil-to-pendulum at two cutting depths

based on the air-run where there were no soil reaction forces to resist in front of the pendulum and slow its motion.

Table 4.6: Maximum soil horizontal and vertical forces from the DEM simulations of soil-to-pendulum

Cutting depth (mm)	Horizontal force (N)	Vertical force (N)	Angle (degree)
25	-365	171	64
50	-766	461	64

Figure 4.10 shows the DEM simulation of soil-to-pendulum at two levels of cutting depth when the pendulum is at 90 degrees from initial horizontal position and has 3.7 m/s linear velocity. As shown in these figures, the DEM soil particles move individually and freely when come in contact with the pendulum. Also, it can be seen that by increasing the cutting depth, the soil surcharge amount and rupture distance in front of the pendulum is increased in DEM simulations.

Table 4.7: Soil horizontal and vertical cutting forces at 90 degrees from DEM simulation of soil-to-pendulum

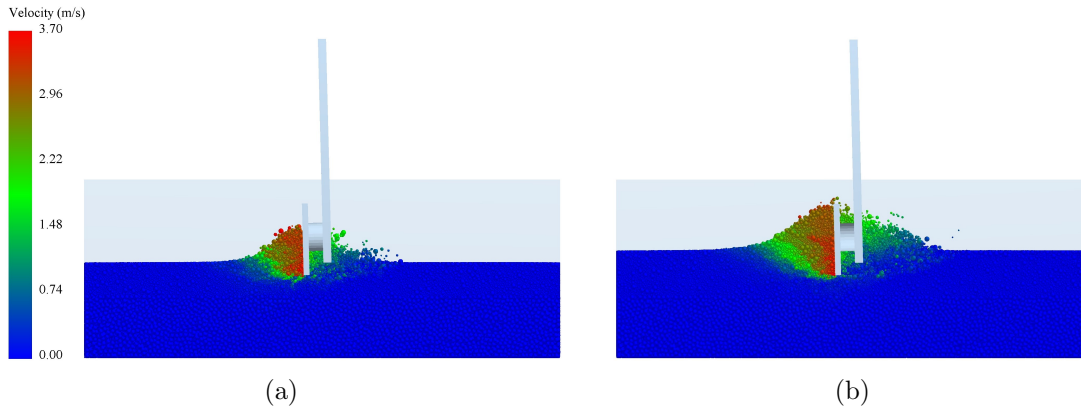| Cutting depth (mm)	Horizontal force (N)	Vertical force (N)
25	-40	-4
50	-98	-4

Figure 4.10: DEM soil flow when pendulum is at 90 degrees from initial position and has 3.7 m/s linear velocity at a) 25 mm and b) 50 mm cutting depths

4.4   DEM-MBD co-simulation of soil-to-pendulum interaction

The position and the angular velocity of the pendulum were analyzed in the DEM-MBD co-simulation since they are affected by the soil reaction forces. As it is shown in Figure 4.11a, at 25 mm cutting depth, the pendulum never reaches 180 degrees because the DEM-MBD coupling captures the effect of the soil reaction forces on the pendulum motion. These resistant forces decrease the velocity of the pendulum, dissipate its energy and prevent it from completing its full cycle. At 25 mm cutting depth, the pendulum reaches 108 degrees in 0.7 seconds of simulation, as in the DEM-only simulation, the pendulum reaches 180 degrees in the same amount of time. At 50 mm cutting depth, the pendulum does not even reach a quarter of the cycle at stops at 66 degrees. The soil resistant forces are so high that prevent the pendulum from further movement. This stop in the pendulum movement can also be seen in Figure 4.11b. The pendulum angular

velocity decreases after contacting with the soil, and reaches zero at 0.5 seconds for 50 mm cutting depth.

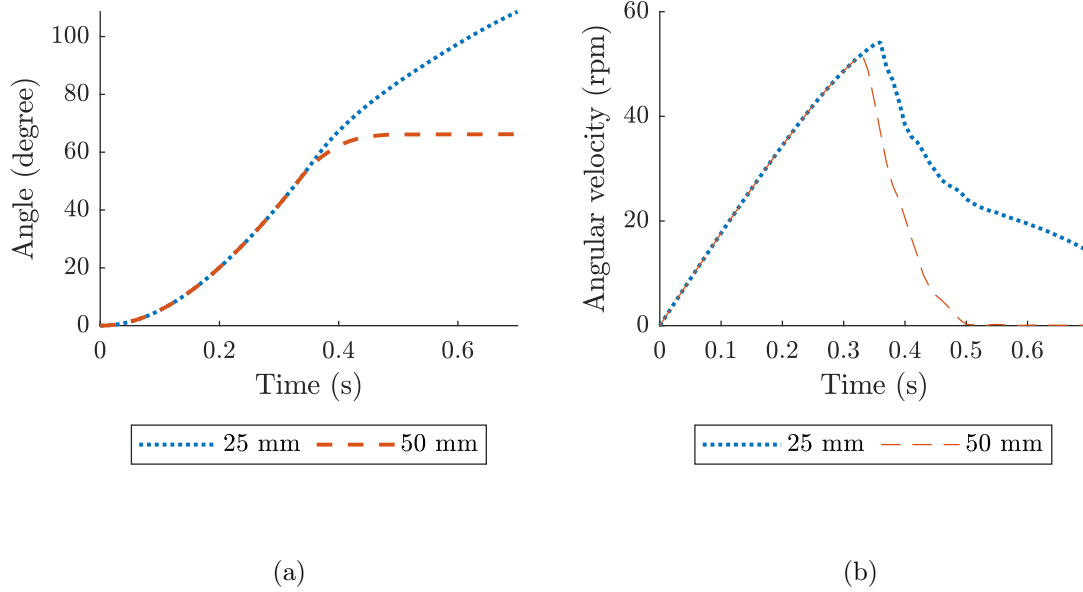(a)   (b)

Figure 4.11: Pendulum a) angle b) and angular velocity from the DEM simulation of soil-to-pendulum interaction at two cutting depths

The horizontal and vertical forces from the soil particles on the cutting plate were directly exported from the EDEM software. As shown in Figure 4.12a, the horizontal soil cutting forces have negative values which represent the compressive force toward the cutting plate. The horizontal force for 50 mm cutting depth is higher than the one for 25 mm cutting depth which matches the same trend as in the experiment of soil-to-pendulum interaction. The pendulum entry angles for the 25 mm and 50 mm cutting depths are 58 degrees and 52 degrees, respectively. As presented in Figure 4.12b, the vertical soil cutting forces are positive which show upward force from the soil. The vertical force for 50 mm cutting depth is also higher than for 25 mm.

The maximum horizontal and vertical forces were determined, and are shown in Table 4.8. Also, the horizontal and vertical forces at 90 degrees from the initial horizontal position are shown in Table 4.9. Similar to both soil-to-pendulum experiment and DEM simulation, the direction of the maximum soil cutting forces are compressive toward the cutting plate for horizontal forces, and upward from the soil for vertical forces. The magnitude of these forces from DEM-MBD co-
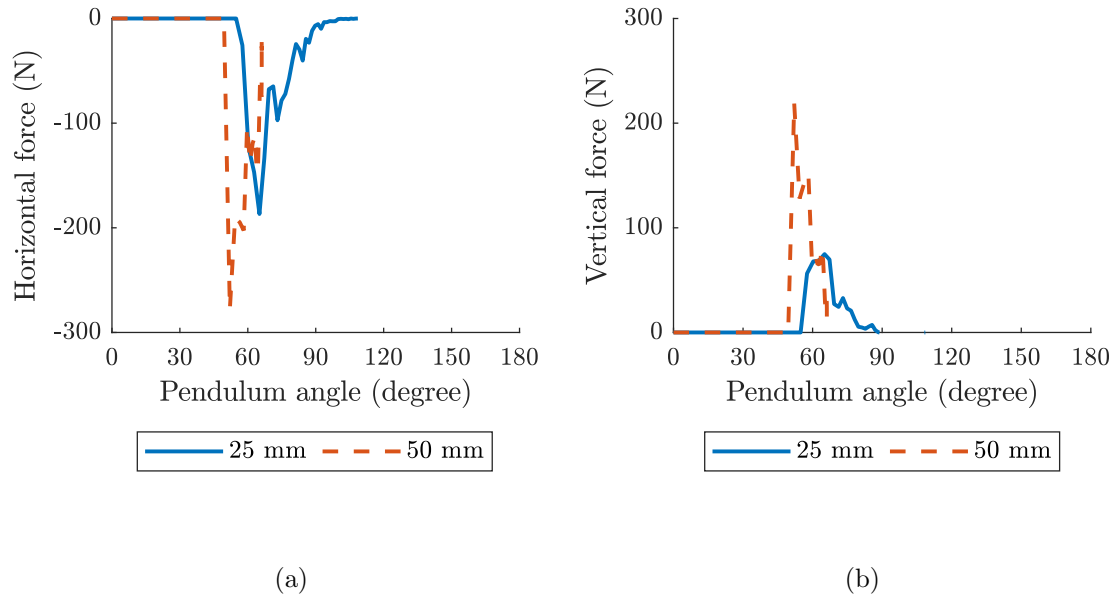
Figure 4.12: Comparison of a) horizontal and b) vertical soil cutting force from the DEM-MBD co-simulation of soil-to-pendulum at two cutting depths

simulation are lower than DEM simulation (Table 4.6) and closer to the experiment (Table 4.1). This change in the magnitude of the horizontal and vertical forces are due to the ability of the DEM-MBD co-simulation to capture the effect of the soil reaction forces on the pendulum motion. In DEM-MBD co-simulation, the reaction forces from the soil particles are determined in the EDEM software and are transfered to the LMS Virtual.Lab Motion software where they are applied to the pendulum as external forces. In LMS, because the horizontal forces are in the opposite direction of the pendulum movement, they decrease the pendulum velocity.

Table 4.8: Maximum soil horizontal and vertical cutting forces from DEM-MBD co-simulation of soil-to-pendulum

Cutting depth (mm)	Horizontal force (N)	Vertical force (N)	Angle (degree)
25	-187	75	65
50	-278	219	52

Figure 4.13a shows the DEM-MBD co-simulation of soil-to-pendulum interaction at time 0.33 seconds, when pendulum is at 90 degrees from initial position and has 1.3 m/s linear velocity at

Table 4.9: Soil horizontal and vertical cutting forces at 90 degrees from the DEM-MBD co-simulation of soil-to-pendulum

Cutting depth (mm)	Horizontal force (N)	Vertical force (N)
25	-7	0
50	-28	10

25 mm cutting depth. The shape of the surcharge is different from the one in DEM simulations as shown in Figure 4.10a. This change is because the pendulum velocity decreases along its movement, but the soil particles keep moving with the same velocity driven by the pendulum in the previous time step. Figure 4.13b DEM-MBD co-simulation of soil-to-pendulum at time 0.47 seconds at 50 mm cutting depth. At this simulation, the pendulum never reaches 90 degrees and stops at 66 degrees. This is due the effect of soil reaction forces on the pendulum motion which was captured by the DEM-MBD coupling technique. Although, this phenomenon does not happen in the soil-to-pendulum experiment and it can be because of the strong bond model between the soil particles in the DEM soil model.
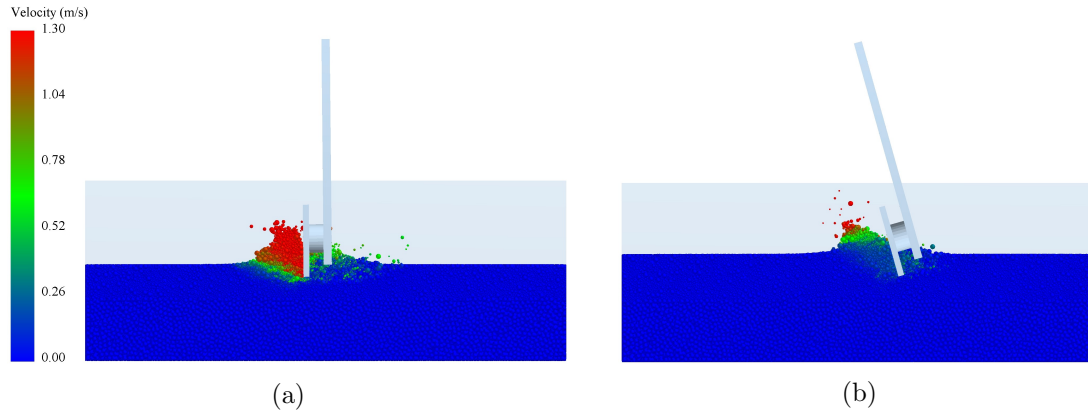

(a)   (b)

Figure 4.13: a) DEM-MBD soil flow when pendulum is at 90 degrees from initial position and has 1.3 m/s linear velocity at 25 mm and b) at equivalent simulation time at 50 mm cutting depth (66 degree and 0.18 m/s linear velocity)

4.5 Comparison of experiment, DEM simulation and DEM-MBD co-simulation of soil-to-pendulum interaction

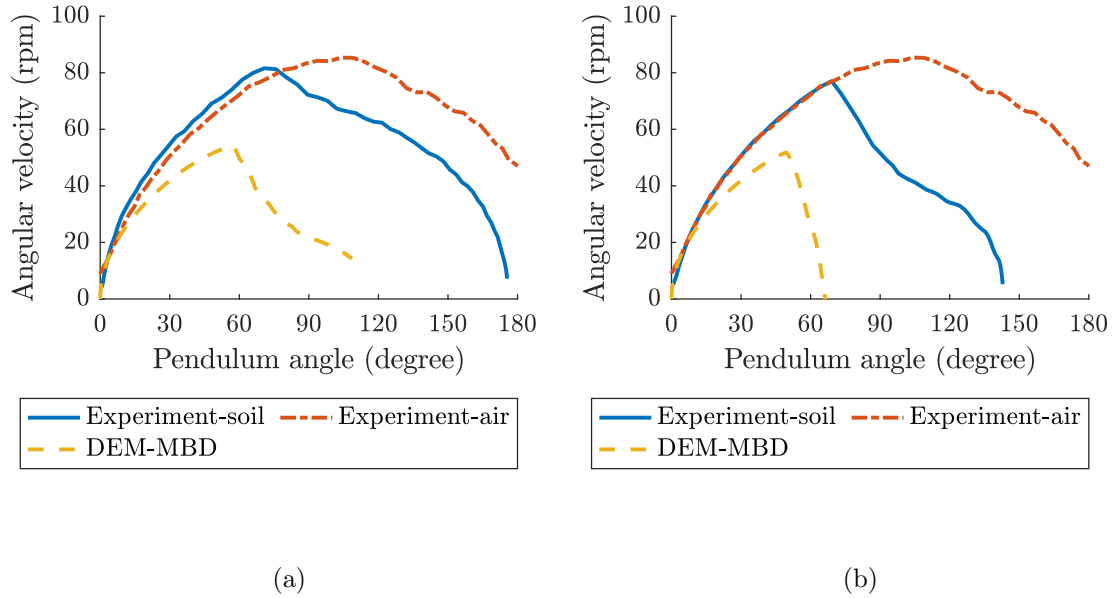(a)   (b)

Figure 4.14: Comparison of pendulum angular velocity from soil-to-pendulum experiment with and without soil interaction, and DEM-MBD co-simulation at a) 25 mm and b) 50 mm cutting depths

Figure 4.14 shows the comparison of pendulum angular velocity from the soil-to-pendulum testwith and without the interaction with soil, and DEM-MBD co-simulation at two cutting depths of 25 mm and 50 mm. The DEM-MBD co-simulation predicted the sudden decrease of the angular velocity, which is due to the sudden interaction of the pendulum with soil. The sudden drop in the angular velocity is more extreme at 50 mm cutting depth due to higher soil reaction forces (Figure 4.14b), which is captured well in DEM-MBD coupling.

Figures 4.15 and 4.16 show the comparison of horizontal and vertical soil cutting forces for the soil-to-pendulum test, DEM simulation, and DEM-MBD co-simulation at two cutting depths of 25 mm and 50 mm. Overall, both horizontal and vertical forces are zero from the starting point to where the pendulum contacts the soil. The horizontal force is negative (which shows compression on the cutting plate) and increases in magnitude when the cutting depth is increased from 25 mm to 50 mm (Figure 4.15). As shown in Figure 4.16, the vertical force is positive which represent the

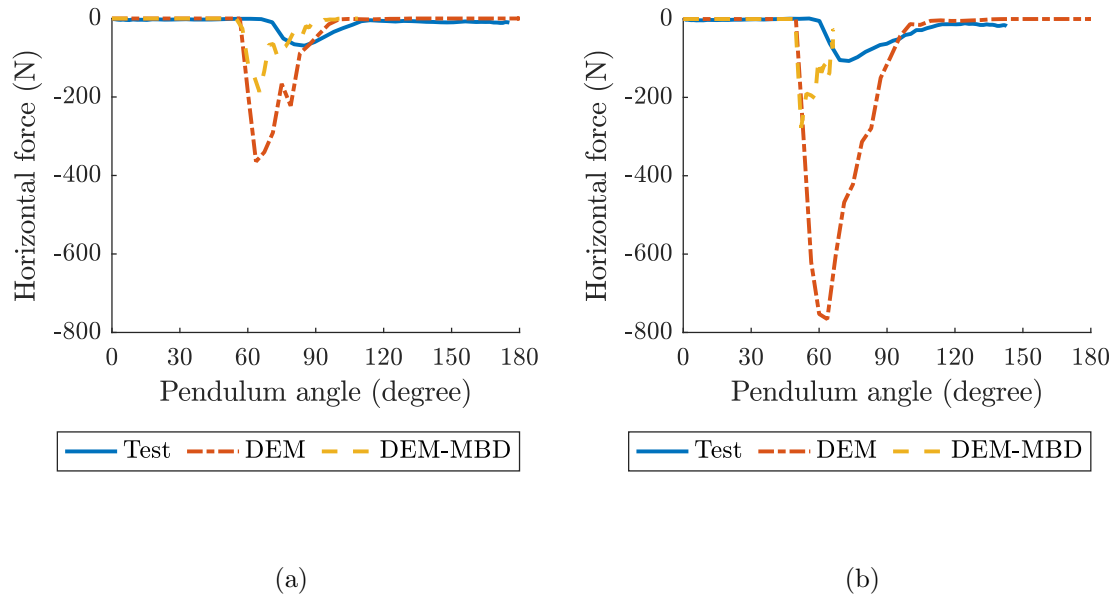(a)   (b)

Figure 4.15: Comparison of horizontal soil cutting forces from soil-to-pendulum experiment, DEM simulation, and DEM-MBD co-simulation at a) 25 mm and b) 50 mm cutting depths

upward force from the soil, and it also increases in magnitude by increasing the cutting depth. This increase in both horizontal and vertical forces are predicted by DEM simulation and DEM-MBD co-simulation; however, the DEM-MBD coupling force prediction is closer to experiment.

Table 4.10 shows the comparison of maximum soil cutting forces from the soil-to-pendulum experiment, DEM only simulation, and DEM-MBD co-simulation. Both DEM and DEM-MBD coupling simulations over-predicted the soil cutting forces. One possible reason is that the DEM parallel bond does not have dampening in addition to the collusion dampening (coefficient of restitution) from particle-to-particle interaction. Secondly, quasi-static cone penetrometer calibration may not have accounted high strain rate effects.

Comparing to DEM only simulation, the DEM-MBD coupling shows a better prediction, and improved the force prediction both for 25 mm and 50 mm cutting depths. This improvement is due to the ability of DEM-MBD co-simulation to capture the effect of the soil reaction forces on the dynamically coupled pendulum motion.

Even though the magnitude of relative errors in predicted soil cutting forces between the DEM-MBD co-simulation and experiment are very high, the trend in predicting the increase in forces
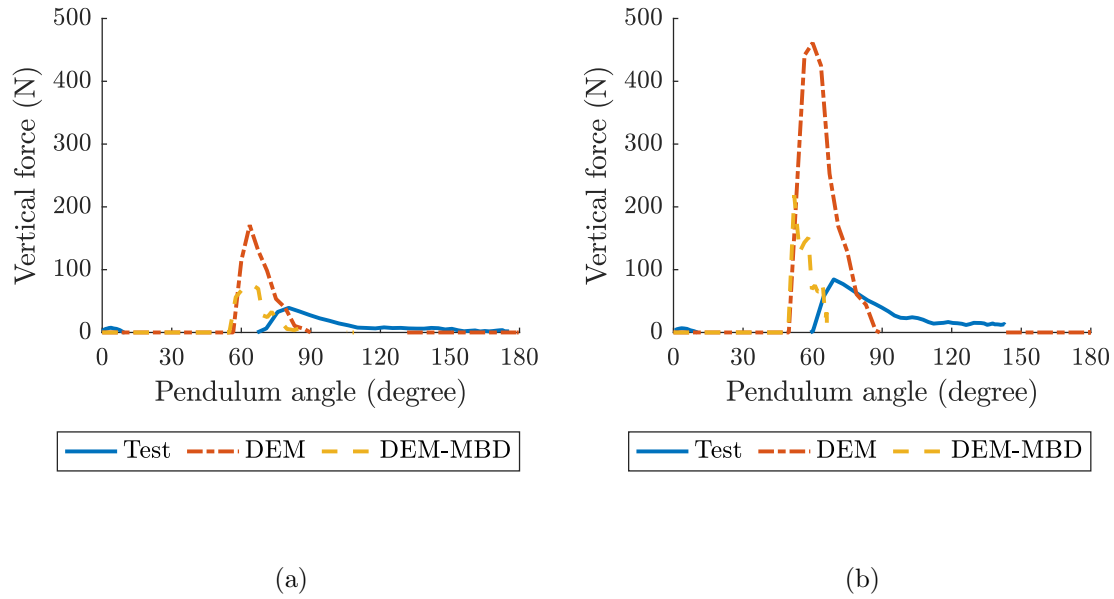
(a)   (b)

Figure 4.16: Comparison of vertical soil cutting forces from soil-to-pendulum experiment, DEM simulation, and DEM-MBD co-simulation at a) 25 mm and b) 50 mm cutting depths

Table 4.10: Comparison of maximum horizontal and vertical soil cutting forces from soil-to-pendulum experiment, DEM simulation, DEM-MBD co-simulation

Soil cutting forces	Horizontal (N)		% increase	Vertical (N)		% increase
Cutting depth	25 mm	50 mm		25 mm	50 mm	
Experiment	-73	-108	48%	38	85	124%
DEM	-365	-766	110%	171	461	170%
DEM-MBD	-187	-278	49%	75	219	192%

by cutting depth was similar to the experiment. The maximum horizontal soil cutting forces from experiment and DEM-MBD co-simulation increase by 48% and 49%, respectively. The DEM only, however, is not able to capture the trend in increased soil cutting forces by cutting depth (109.8% increase in maximum horizontal soil cutting force from 25 mm to 50 mm cutting depth).

CHAPTER 5. CONCLUSION

The soil-to-tool interaction application was successfully modeled using DEM and DEM-MBD coupling techniques to predict the soil reaction forces from the soil cutting tool with a pendulum motion. Several laboratory tests (particle size distribution, compaction proctor, direct shear and triaxial tests) were performed on the loam (33 sand, 45 silt, 22 clay) soil to characterize its mechanical properties to be used for initialization and calibration of DEM soil model parameters.

To calibrate the DEM soil model, the cone penetrometer and angle of repose tests were used sequentially to calibrate the DEM parameters of coefficients of static friction and rolling friction, shear modulus and bond stiffness (related to bond contact model). Both cone penetrometer and angle of repose tests were simulated in EDEM, a commercial DEM code, using the design of experiment (DOE) for the DEM input parameters. Using the calibrated values, DEM predicted the steady state soil cone index from the cone penetrometer test and soil angle of repose with relative errors of 11%, and 24%, respectively.

A simple test was developed for validation of the DEM soil-to-tool interaction model which included a simple pendulum. This pendulum had a cutting blade (153 mm height and 101 mm width) mounted in front of its linkage arm. The pendulum with a revolute joint was released from the horizontal position and dynamically cut through the soil bed underneath it. The tests were conducted at 25 mm and 50 mm cutting depth. The soil reaction forces (normal and tangential) on the pendulum linkage, and the position and angular velocity of the pendulum was measured. High-speed video frames were also captured to qualitatively evaluate the soil flow from the pendulum tests.

The soil-to-pendulum test was modeled using DEM and DEM-MBD coupling in order to compare the outcome of these two methods to the results of the physical test. Both simulation approaches, DEM only and DEM-MBD, over-predicted the soil reaction forces (horizontal and verti-

cal); however, the DEM-MBD co-simulations had a closer outcome comparing to the physical test. Utilizing DEM-MBD coupling improved the prediction of soil cutting forces. This improvement could be due to capturing the effect of the soil reaction forces and relative soil particle flow from the pendulum motion in the DEM-MBD co-simulation. In addition, DEM-MBD co-simulation showed better qualitatively soil flow from the dynamically moving pendulum blade compared to the DEM only.

It is generally concluded that due to the discreteness of DEM, the soil dynamic responses can be predicted more accurately using the DEM technique. Also, DEM can predict reaction forces from individual particles which result in a force distribution implemented on the tool. This case study showed that if DEM is coupled with other numerical methods, it can be advantageous for improvement of the simulation-based design process for various applications.

5.1 Future research

Future research is needed to improve the force prediction from the DEM-MBD simulation of the soil-to-pendulum system. New experiments should be evaluated for calibration of DEM soil model that have high strain rate. Other DEM contact models can also be explored to improve the prediction of forces. For instance, contact models that capture the elasto-plastic and dynamic damping behavior of soil may be needed. The soil-to-pendulum interaction can be integrated into a DOE calibration methodology to account for high strain rate effects. A machine scale size such as tillage tools (like rotary tillers), planters (especially the furrow opener section), construction machinery (loader bucket), tire-to-soil interaction, and turf grass aeration equipment can be used as a validation application.

BIBLIOGRAPHY

ASABE Standard (1999). Procedures for using and reporting data obtained with the soil cone penetrometer (EP542).

ASAE Standard (1999). Soil cone penetrometer (ASAE S313.3).

Asaf, Z., Rubinstein, D., and Shmulevich, I. (2007). Determination of discrete element model parameters required for soil tillage. *Soil and Tillage Research*, 92(1-2):227–242.

ASTM International (2000). Standard test method for measuring the angle of repose of free-flowing mold (C1444-00).

ASTM International (2001a). Standard Test Method for Ash in Biomass (E1755-01).

ASTM International (2001b). Standard test method for pH of soils (D4972-01).

ASTM International (2010). Standard test method for liquid limit, plastic limit, and plasticity index of soils (D4318-10).

ASTM International (2011a). Standard test method for consolidated undrained triaxial compression test for cohesive soils (D4767-11).

ASTM International (2011b). Standard test method for direct sheartest of soils under consolidated drained conditions (D3080/D3080M-11).

ASTM International (2012). Standard test method for laboratory compaction characteristics of soil using standard effort (D698-12).

ASTM International (2014). Standard test method for specific gravity of soil solids by water pycnometer (D854-14).

ASTM International (2017a). Standard test method for particle-size distribution (Gradation) of fine-grained soils using the sedimentation (hydrometer) analysis (D7928).

ASTM International (2017b). Standard test method for particle-size distribution (gradation) of soils using sieve analysis (D6913/D6913M-17).

Belheine, N., Plassiard, J. P., Donzé, F. V., Darve, F., and Seridi, A. (2009). Numerical simulation of drained triaxial test using 3D discrete element modeling. *Computers and Geotechnics*, 36:320–331.

Chancellor, W. J. (1994). Soil physical properties. *American Society of Agricultural and Biological Engineers*, 3:21–245.

Chen, H., Liu, Y. L., Zhao, X. Q., Xiao, Y. G., and Liu, Y. (2015). Numerical investigation on angle of repose and force network from granular pile in variable gravitational environments. *Powder Technology*, 283:607–617.

Chen, Y., Munkholm, L. J., and Nyord, T. (2013). A discrete element model for soil-sweep interaction in three different soils. *Soil and Tillage Research*, 126:34–41.

Chi, L. and Kushwaha, R. L. (1990). A non-linear 3-D finite element analysis of soil failure with tillage tools. *Journal of Terramechanics*, 27:343–366.

Chi, L., Tessier, S., and Lague, C. (1993). Finite element prediction of soil compaction induced by various running gears. *Transactions of the ASABE*, 36:629–636.

Chou, H. T., Lee, C. F., Chung, Y. C., and Hsiau, S. S. (2012). Discrete element modelling and experimental validation for the falling process of dry granular steps. *Powder Technology*, 231:122–134.

Coetzee, C. J. (2016). Calibration of the discrete element method and the effect of particle shape. *Powder Technology*, 297:50–70.

Coetzee, C. J. (2017). Review: Calibration of the discrete element method. *Powder Technology*, 310:104–142.

Coetzee, C. J. and Els, D. N. J. (2009). Calibration of discrete element parameters and the modelling of silo discharge and bucket filling. *Computers and Electronics in Agriculture*, 65(2):198–212.

Combarros, M., Feise, H. J., Zetzener, H., and Kwade, A. (2014). Segregation of particulate solids: Experiments and DEM simulations. *Particuology*, 12(1):25–32.

Craig, R. (2004). *Craig's soil mechanics*. Spon Press.

Cundall, P. A. and Strack, O. (1979). A discrete numerical model for granular assemblies. *Geotechnique*, 29(1):47–65.

DEM Solutions Ltd (2014). EDEM 2.6 theory reference guide.

Derakhshani, S. M., Schott, D. L., and Lodewijks, G. (2015). Micro-macro properties of quartz sand: Experimental investigation and DEM simulation. *Powder Technology*, 269:127–138.

D'Errico, J. (2017). Shape Language Modeling. *MATLAB Central File Exchange*.

Duncan, J. M. and Chang, C. (1970). Nonlinear analysis of stress and strain in soilds. *Journal of Soil Mechanics and Foundations Divisions*, 89:1629–1653.

Gill, W. R. and Berg, G. E. V. (1968). *Soil dynamics in tillage and traction*. United States Department of Agriculture.

Godwin, R. J. (2007). A review of the effect of implement geometry on soil failure and implement forces. *Soil and Tillage Research*, 97(2):331–340.

Godwin, R. J. and Spoor, G. (1977). Soil failure with narrow tines. *Journal of Agricultural Engineering Research*, 22(3):213–228.

González-Montellano, C., Fuentes, J. M., Ayuga-Téllez, E., and Ayuga, F. (2012). Determination of the mechanical properties of maize grains and olives required for use in DEM simulations. *Journal of Food Engineering*, 111(4):553–562.

Hertz, H. (1882). On the contact of elastic solids. *Journal für die reine und angewandte Mathematik*, 92:156–171.

Hettiaratchi, D. R. and Reece, A. R. (1967). Symmetrical three-dimensional soil failure. *Journal of Terramechanics*, 4(3):45–67.

Hettiaratchi, D. R. P., Witney, B. D., and Reece, A. R. (1966). The calculation of passive pressure in two-dimensional soil failure. *Journal of Agriculture Engineering Research*, 11:89–107.

Hogue, C. (1998). Shape representation and contact detection for discrete element simulations of arbitrary geometries. *Engineering Computations*, 15(3):374 – 390.

Höhner, D. and Wirtz, S.Scherer, V. (2012). Experimental and numerical investigation on the influence of particle shape and shape approximation on hopper ischarge using discrete element method. *Powder Technology*, 235(8):614–627.

Hu, Y. K. and Abeels, P. F. J. (1994). Agricultural tire deformation in the 2D case by finite element method. *Journal of Terramechanics*, 31(6):353–370.

Larson, L. W., Lovely, W. G., and Bockhop, C. W. (1968). Predicting draft forces using model moldboard plows in agricultural soils. *Transactions of the ASAE*, 11:665–668.

Li, Q., Feng, M., and Zou, Z. (2013). Validation and calibration approach for discrete element simulation of burden charging in pre-reduction shaft furnace of COREX process. *ISIJ International*, 53(8):1365–1371.

Li, Y., Xu, Y., and Thornton, C. (2005). A comparison of discrete element simulations and experiments for 'sandpiles' composed of spherical particles. *Powder Technology*, 160(3):219–228.

Liu, C. H. and Wong, J. Y. (1996). Numerical simulations of tire-soil interaction based on critical state soil mechanics. *Journal of Terramechanics*, 33(5):209–221.

Luth, H. J. and Wismer, R. D. (1971). Performance of plane soil cutting blades in sand. *Transactions of the ASAE*, 15(2):0211–0216.

Mckyes, E. (1985). *Soil cutting and tillage.* Elsevier Science Publishers.

McKyes, E. and Ali, O. S. (1977). The cutting of soil by narrow blades. *Journal of Terramechanics*, 14(2):43–58.

Mindlin, R. D. (1949). Compliance of elastic bodies in contact. *Journal of Applied Mechanics*, 16:259 – 268.

Mindlin, R. D. and Deresiewicz, H. (1953). Elastic spheres in contact under varying oblique forces. *Journal of applied mechanics*, 20:327 – 344.

Mousaviraad, M., Tekeste, M. Z., and Rosentrater, K. A. (2017). Calibration and validation of a discrete element model of corn using grain flow simulation in a commercial screw grain auger. *Transactions of the ASABE*, 60(4):1403–1415.

Nakashima, H. and Wongt, J. Y. (1993). A three-dimensional tire model by the finite element method. *Journal of Terramechanic*, 30(1):21–34.

Obermayr, M., Dressler, K., Vrettos, C., and Eberhard, P. (2011). Prediction of draft forces in cohesionless soil with the discrete element method. *Journal of Terramechanics*, 48:347–358.

Osman, M. (1964). The mechanics of soil cutting blades. *Journal of Agricultural Engineering Research agric. Engng Res*, 9:313–328.

O'Sullivan, C. (2011). *Particulate discrete element modeling*. Spon Press.

Payne, P. C. J. (1956). The relationship between the mechanical properties of soil and the performance of simple cultivation implement. *Journal of Agricultural Engineering Research*, 1:23–50.

Plouffe, C., Lague, C., Tessier, S., Richard, M. J., and Mclaughlin, N. B. (1999a). Moldboard plow performance in a clay soil: simulation and experiment. *Transactions of the ASAE*, 42(6):1531–1539.

Plouffe, C., Richard, M. J., Tessier, S., and Lague, C. (1999b). Validation of moldboard plow simulations with FEM on a clay soil. *Transactions of the ASAE*, 42(6):1523–1529.

Potyondy, D. O. and Cundall, P. A. (2004). A bonded-particle model for rock. *International Journal of Rock Mechanics and Mining Sciences*, 41(8 SPEC.ISS.):1329–1364.

Rankine, W. J. M. (1857). On the stability of loose earth. *Philosophical Transaction of the Royal Society*, 147:9–27.

Raper, R. L. and Erbach, D. C. (1990). Prediction of soil stresses using the finite element method. *Transactions of the ASAE*, 33(3):725–730.

Reece, A. R. (1965). The fundamental equation of earth-moving mechanics. *Institution of Mechanical Engineers*, 179:16–22.

Sakaguchi, H., Ozaki, E., and Igarashi, T. (1993). Plugging of the flow of granular materials during the discharge from a silo. *International Journal of Modern Physics*, 7(9 & 10):1949 – 1963.

SAS Institute Inc (2018). JMP 14 profilers.

Shoop, S. (1993). Terrain characterization for trafficability. *US Army Corps and Engineers*.

Soehne, W. (1956). Some principles of soil mechanics as applied to agricultural engineering. *Grundlagen der Landtechnik*, 7:11–27.

Swick, W. C. and Perumpral, J. V. (1988). A model for predicting soil-tool interaction. *Journal of Terramechanics*, 25(1):43–56.

Tamás, K., Jóri, I. J., and Mouazen, A. M. (2013). Modelling soil-sweep interaction with discrete element method. *Soil and Tillage Research*, 134:223–231.

Tekeste, M. Z., Balvanz, L. R., Hatfield, J. L., and Ghorbani, S. (2019). Discrete element modeling of cultivator sweep-to-soil interaction: Worn and hardened edges effects on soil-tool forces and soil flow. *Journal of Terramechanics*, 82:1–11.

Tekeste, M. Z., Mousaviraad, M., and Rosentrater, K. A. (2018). Discrete element model calibration using multi-responses and simulation of corn flow in a commercial grain auger. *Transactions of the ASABE*, 61(5):1743–1755.

Terzaghi, K. (1943). *Theoretical soil mechanics*. John Wiley and Sons Inc.

Tsuji, Y., Tanaka, T., and Ishida, T. (1992). Langrangian numerical simulation of plug flow of cohesionless particles in a horizontal pipe. *Powder Technology*, 71:239–250.

Ucgul, M., Fielke, J. M., and Saunders, C. (2014). Three-dimensional discrete element modelling of tillage: Determination of a suitable contact model and parameters for a cohesionless soil. *Biosystems Engineering*, 121:105–117.

Upadhyaya, S. K., Rosa, U. A., and Wulfsohn, D. (2002). Application of the finite element method in agricultural soil mechanics. *Advances in Soil Dynamics*, 2:117–153.

Vilde, A. (2003). Up-to-date trends in soil tillage engineering. *Polish Academy of Sciences Branch in Lublin. TEKA Commision of Motorization and Power Industry in Agriculture*, pages 257–262.

Wang, L., Zhou, W., Ding, Z., Li, X., and Zhang, C. (2015). Experimental determination of parameter effects on the coefficient of restitution of differently shaped maize in three-dimensions. *Powder Technology*, 284:187–194.

Wismer, R. D. and Luth, H. J. (1972). Performance of plane soil cutting blades in clay. *Transactions of the ASAE*, 15(2):211–216.

Yong, R. N. and Hanna, A. W. (1977). Finite element analysis of plane soil cutting. *Journal of Terramechanics*, 14(3):103–125.